Factors Controlling Low-Cloud Evolution over the Eastern Subtropical Oceans: A Lagrangian Perspective Using the A-Train Satellites

RYAN EASTMAN AND ROBERT WOOD

Department of Atmospheric Sciences, University of Washington, Seattle, Washington

(Manuscript received 10 July 2015, in final form 8 September 2015)

ABSTRACT

A Lagrangian technique is developed to sample satellite data to quantify and understand factors controlling temporal changes in low-cloud properties (cloud cover, areal-mean liquid water path, and droplet concentration). Over 62 000 low-cloud scenes over the eastern subtropical/tropical oceans are sampled using the A-Train satellites. Horizontal wind fields at 925 hPa from the ERA-Interim are used to compute 24-h, two-dimensional, forward, boundary layer trajectories with trajectory locations starting on the *CloudSat*/*CALIPSO* track. Cloud properties from MODIS and AMSR-E are sampled at the trajectory start and end points, allowing for direct measurement of the temporal cloud evolution. The importance of various controls (here, boundary layer depth, lower-tropospheric stability, and precipitation) on cloud evolution is evaluated by comparing cloud evolution for different initial values of these controls. Viewing angle biases are removed and cloud anomalies (diurnal and seasonal cycles removed) are used throughout to quantify cloud evolution relative to the climatological-mean evolution. Cloud property anomalies show temporal changes similar to those expected for a stochastic red noise process, with linear relationships between initial anomalies and their mean 24-h changes. This creates a potential bias when comparing the evolutions of sets of trajectories with different initial anomalies; three methods are introduced and evaluated to account for this. Results provide statistically robust observational support for theoretical/modeling studies by showing that low clouds in deep boundary layers and under weak inversions are prone to break up. Precipitation shows a more complex and less statistically significant relationship with cloud breakup. Cloud cover in shallow precipitating boundary layers is more persistent than in deep precipitating boundary layers. Liquid water path and cloud droplet concentration decrease more rapidly for precipitating clouds and in deep boundary layers.

1. Introduction

Subtropical marine stratocumulus (Sc) clouds cool Earth's climate significantly. Stratocumulus clouds radiate at temperatures nearly as warm as the sea surface, while they reflect much of the abundant sunlight in the subtropics (Hartmann and Short 1980). The massive extent of subtropical Sc decks combined with their strong cooling influence makes it essential that we understand the nature of their formation, mesoscale variability, physical processes, and eventual dissipation (Wood 2012). In this work we establish a Lagrangian framework following individual cloud samples within the planetary boundary layer (PBL) over one complete diurnal cycle in order to test the effects of several known or hypothesized cloud-controlling variables.

Stratocumulus clouds in subtropical decks undergo a life cycle lasting several days. Bretherton and Wyant (1997) explained key aspects of the marine PBL structure and consequences for cloud evolution using a mixed layer model. Quasi-permanent subtropical high pressure systems advect air from the cool eastern subtropical oceans to regions with warmer sea surface temperatures. Marine Sc form in the shallow, cool PBL that forms immediately offshore. Cloud tops emit longwave radiation upward, cooling the air at the cloud top, and driving overturning of the entire PBL (Lilly 1968; Nicholls 1989). The PBL is characterized as ''coupled'' or ''well mixed'' when the radiatively driven circulation spans from cloud top to the sea surface. As the Sc is advected farther offshore and equatorward, entrainment of warm dry air at the cloud top combines with increased latent heating from warming sea surface temperatures (SSTs) to deepen the PBL (Randall 1984; Krueger et al. 1995;

Corresponding author address: Ryan Eastman, Department of Atmospheric Sciences, University of Washington, Box 351640, Seattle, WA 98195.
E-mail: rmeast@atmos.washington.edu

DOI: 10.1175/JAS-D-15-0193.1

Wyant et al. 1997). Eventually, the PBL can become sufficiently deep to prevent the negatively buoyant parcels at the cloud top from reaching the surface, creating a cloud layer that is ''decoupled'' from the sea surface. The mixed layer beneath the Sc-containing layer continues to moisten, and cumulus (Cu) clouds eventually form atop the mixed layer, protruding into the Sc deck. The Sc deck eventually breaks up and is replaced by the underlying Cu. There is a pronounced diurnal cycle within this system favoring coupled PBLs and more extensive cloud cover at night (Turton and Nicholls 1987; Rogers and Koracin 1992; Eastman and Warren 2014).

Prior studies show that numerous processes may act to prolong or shorten the transition from Sc to Cu and that cloud-controlling variables are frequently correlated. Sc amount in the northeast Pacific Ocean was shown by Klein et al. (1995) to be dependent upon sea surface temperature and 750-hPa temperature 24–30 h upstream of the sampling location. Using a large-eddy simulation (LES), Sandu and Stevens (2011) showed that the pace of the Sc–Cu transition is primarily dictated by the strength of the temperature inversion at the beginning of the process, although they did not explore the range of meteorological phase space that exists in nature. Their simulations also suggest that precipitation and reduced cloud-top cooling caused by increased downwelling IR above the cloud deck can hasten the Sc–Cu transition. Xiao et al. (2011), also using LES, concluded that PBL decoupling due to surface evaporation is an important factor in Sc breakup. Wood and Bretherton (2004) used satellite data to show that strong entrainment is associated with deeper PBLs and that deeper PBLs are far more likely to be decoupled. Wood and Hartmann (2006) also used satellite data to show that PBL depth plays a significant role in the physical and radiative properties of marine Sc. Zhou et al. (2015) used field data from the Marine ARM GCSS Pacific Cross-Section Intercomparison (GPCI) Investigation of Clouds (MAGIC) campaign over the northeast Pacific to show that Sc breakup occurs downwind of decoupling and suggested that the primary driver of decoupling is dry-air entrainment at the top of the cloud layer, while precipitation processes and surface latent heating were less impactful. Mauger and Norris (2010) used a Lagrangian approach to find that a proxy for PBL decoupling and weak lower-tropospheric stability (LTS) preceding observation both lead to reductions in cloud cover. Myers and Norris (2013) used satellite cloud data and reanalyses to show that stronger inversions lead to reduced entrainment and more persistent clouds and that increased large-scale subsidence shallows the PBL, leading to fewer, thinner clouds.

Precipitation processes within Sc are complex, and there is no general consensus about how precipitation affects cloud and PBL evolution. Stevens et al. (1998) showed that precipitation suppresses PBL turbulence and can reduce the cloud liquid water path (LWP). However, suppression of turbulence will reduce cloud-top entrainment and might slow down the decoupling transition. The model developed by Bretherton and Wyant (1997) shows that drizzle acts as a stabilizing force within the PBL, where condensing water vapor releases latent heat at cloud top and evaporating rain cools the subcloud layer. They concluded that rain promotes decoupling in Sc decks—a conclusion first suggested by Nicholls (1984) and Wang and Albrecht (1986) and later substantiated by Mechem and Kogan (2003) using a coupled ocean–atmosphere model. Stevens et al. (2005) and Comstock et al. (2005) used field data to show that precipitation may lead to increased cloud-cover variability and the development of ''pockets of open cells'' (POCS); however, Burleyson and Yuter (2015) showed that cloud temporal changes over 1–3 h are not particularly sensitive to precipitation.

Klein et al. (1995) concluded that the Lagrangian histories of Sc within the marine PBL must be accounted for in order to understand how clouds evolve. Pincus et al. (1997), Sandu et al. (2010), and Mauger and Norris (2010) have carried out successful Lagrangian studies using wind fields from model reanalysis and composited satellite cloud data. Here, we use A-train satellite data and environmental data from the reanalysis of the European Centre for Medium-Range Weather Forecasts (ECMWF) to follow 62 000 individual trajectories within subtropical Sc regions over a 24-h period. We group trajectories by the values of factors potentially controlling cloud evolution to test whether cloud evolution is sensitive to these factors.

2. Data selection

a. *Using surface observations to select regions for study*

Stratocumulus clouds are most prevalent in regions of large-scale subsidence over the subtropical eastern ocean basins, and their breakup is critical for setting the tropical albedo. Trajectory start points for this study (red boxes in Fig. 1) are from the cool eastern subtropical/tropical ocean regions where Sc clouds dominate. Within these regions we follow individual cloud scenes in easterly (offshore) flow under subtropical high pressure ridges. We do not include midlatitude regions in this study.

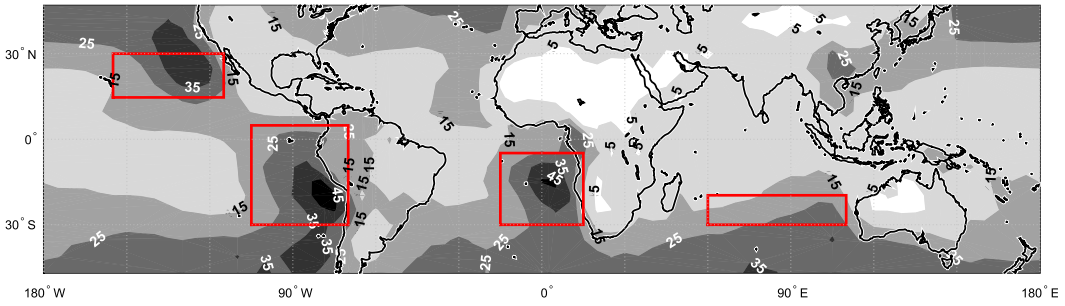

FIG. 1. A smoothed contour plot showing the yearly average, daytime mean Sc amount (%) between 45°N and 45°S from surface observations of stratocumulus clouds (Hahn and Warren 2007). Ocean data are the average for the period 1954–97 and land data are for the period 1971–96. Cloud amount is reported by surface observers either on ships or at weather stations. The red boxes show our regions of study. We use only the ocean portions of the boxes.

Regions were chosen using a 10° × 10° grid of long-term average, yearly mean, daytime Sc cloud amounts from Hahn and Warren (2007). The box boundaries shown in Fig. 1 represent the maximum extent of +1-sigma or greater mean Sc amounts in each of the four regions. Boxes were cut off at 30° latitude to exclude midlatitude regions.

b. Calculating and sampling trajectories

We use the wind fields from the ECMWF interim reanalysis (ERA-Interim) dataset (Dee et al. 2011) to produce ~62 000 individual trajectories for all months during the years 2007 and 2008. Our two-dimensional forward trajectories are calculated using the same routine as in Bretherton et al. (2010, their Figs. 9c and 9d)—that is, using horizontal wind fields at 925 hPa (i.e., within the PBL) with a spatial resolution of 0.75°. Each trajectory begins at a point along the *CloudSat* and *CALIPSO* tracks. Points are chosen randomly along the track, and must be at least 200 km apart. We sample along the ascending and descending satellite tracks, so our collection of trajectories includes 24-h changes from day to day and from night to night. We include only westward-propagating trajectories to eliminate the influence of eastward-moving weather systems; this eliminates about 16% of our observations.

Initial cloud samples are observed with *CloudSat*, *CALIPSO*, MODIS, and AMSR-E (all introduced in their own sections below) within a 100-km radius of the trajectory start point. We then sample the same cloud systems 12 and 24 h later, within a circle of 100-km radius about the advecting trajectory location. The trajectory end points are sampled only with MODIS and AMSR-E, as those instruments scan through sufficiently wide viewing angles, increasing the likelihood that trajectories of varying distances will be resampled. Figure 2 shows an example trajectory, the mean winds, the radii sampled, the initial *CloudSat*/*CALIPSO* and *Aqua* subsatellite tracks, and the MODIS swaths at 0, 12, and 24 h.

c. Cloud-controlling variables

1) LOWER-TROPOSPHERIC STABILITY

We use the *CloudSat* ECMWF auxiliary dataset to calculate the LTS for all of our initial samples. We define LTS as the difference in potential temperature between 700 hPa and the 2-m air temperature.

2) PRECIPITATION FROM *CLOUDSAT*

Precipitation data come from the *CloudSat* 2C-RAIN-PROFILE product (Mitrescu et al. 2010; Lebsock and L'Ecuyer 2011). *CloudSat* uses a 94-GHz nadir-looking cloud profiling radar with a resolution of 1.7 km along track, 1.4 km cross track, and 500 m in the vertical. The RAIN-PROFILE product contains a ''precip_flag'' variable that specifies whether a given radar shot samples near-surface precipitation. We classify a 200-km-long sample of the *CloudSat* track surrounding the trajectory start point as ''precipitating'' if surface precipitation is detected in one or more shots; otherwise the sample is labeled as ''not precipitating.'' We calculate a precipitation frequency variable for each sample as the percentage of profiles within a 200-km-long sample with detectable near-surface precipitation.

CloudSat also offers a ''rain_rate'' variable, measuring the intensity of precipitation reaching the surface. We multiply the intensity and frequency to create a sample rain-rate variable to represent the mean rain rate falling over the entire 200-km sample.

The *CloudSat* swath samples only a narrow cut (curtain) through our sampling circle. To test whether a cut through a radar image is representative of the areal average precipitation we use scanning C-band radar data from the Eastern Pacific Investigation of Climate

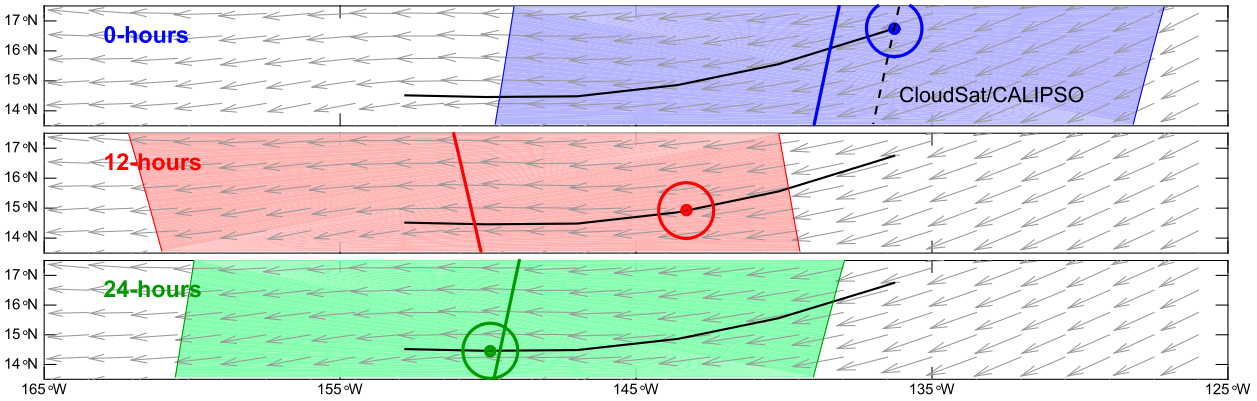

FIG. 2. An example 30-h trajectory from the northeast Pacific beginning 1059 UTC 6 Jan 2007. The trajectory is shown in black. The gray arrows represent the mean wind field at 925 hPa. (top) The black dashed line shows the *CloudSat/CALIPSO* track. The 100-km sampling radius is shown by the circles in each frame. The *Aqua* satellite track (carrying both MODIS and AMSR-E instruments) is shown by the solid colored lines. The MODIS swath is shown by the colored regions surrounding the *Aqua* track. Only MODIS data from *Aqua* are used.

(EPIC; Bretherton et al. 2004), which took place in our southeastern Pacific box (Fig. 1).

The *CloudSat* radar is able to estimate near-surface precipitation rates as low as ~0.0015 mm h^{-1} (0.04 mm day^{-1}) according to a frequency distribution of rain rates (per shot) for one month of data, corresponding to a near-surface radar return of approximately −15 dB*Z* (Comstock et al. 2004; *Z–R* relationship from their Fig. 1). Using 1670 EPIC C-band radar images (60-km diameter) we compare the precipitation frequency derived from a single cut to that from the entire area of each image using a threshold reflectivity of −15 dB*Z*. There is a tight relationship (not shown) between cut and area averages with a correlation coefficient of 0.91 and a slope very close to unity, demonstrating that *CloudSat* cuts can represent areal average frequencies. For higher-reflectivity thresholds (e.g., 0 dB*Z*), the cut-vs-area relationship is less tight but still retains a correlation coefficient of 0.84. Given that cut-based estimates explain two-thirds or more of the variance in areally derived precipitation frequency, we are confident that *CloudSat* is able to estimate precipitation frequency for our trajectory start point samples.

3) DETERMINING CLOUD-TOP HEIGHT WITH *CALIPSO*

We use the Vertical Feature Mask product (VFM; Vaughan et al. 2004) based on lidar backscatter data from the Cloud–Aerosol Lidar with Orthogonal Polarization (CALIOP) on the *Cloud–Aerosol Lidar and Infrared Pathfinder Satellite Observations* (*CALIPSO*) to infer PBL depth at the beginning of each trajectory. CALIOP samples are more or less collocated with *CloudSat* samples. We restrict CALIOP data to the lowest 3 km only, where each individual CALIOP profile represents a 90-m-long footprint separated by 330 m. Each 200-km-long sample collocated with *CloudSat* contains ~600 individual VFM profiles. For Sc fields, the cloud tops sit just below the base of the inversion delineating the PBL top, and for Cu fields the highest Cu cloud tops sit at or below the trade inversion. For each individual lidar profile, the altitude of the highest "cloud" return within the lowest 3 km is used and is combined with the other lidar profiles in the sample to estimate a single value of PBL depth for the entire sample. In some cases this is straightforward (e.g., Fig. 3a), while in other cases it is more challenging to discern as shown in Fig. 3b. The red line indicates the PBL depth assigned to the samples in Fig. 3a and 3b. To determine the PBL depth for each sample, we use the distribution of cloud-top heights within the sample (e.g., Fig. 3c). This distribution may contain multiple peaks, indicating multiple cloud-top maxima within the sample. Peaks within the distribution are considered relevant if they are at least 40% as populated as the largest peak. The PBL depth for the sample is assigned to the relevant peak with the highest altitude. In the case of Fig. 3c the largest peak is also the highest relevant peak, at around 1.9 km. We choose this method in order to minimize the number of cases where we assign cloud tops to trade cumulus coinciding with small amounts of remaining overlying Sc. The 40% threshold was chosen as most suitable after visual inspection of hundreds of samples using a variety of thresholds. If no clouds are present in the sample (<5% of samples) the PBL depth cannot be determined and no value is assigned. Samples with unassigned PBL depths are used only in analyses that do not take PBL depth into account.

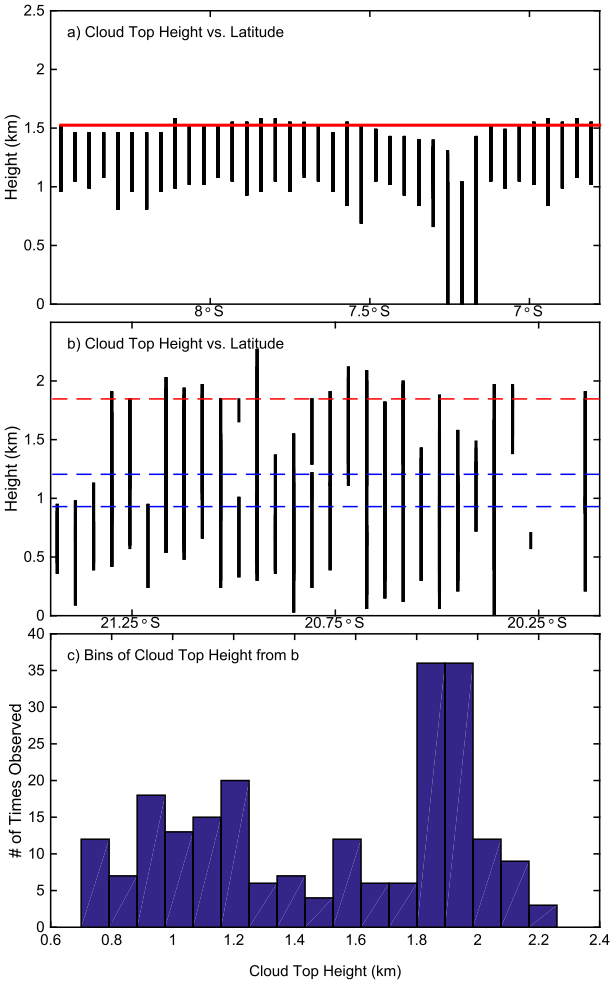

FIG. 3. (a),(b) Plots of *CALIPSO* VFM "cloud" returns within the marine boundary layer for two separate samples. The red lines [dashed in (b)] indicate the cloud-top height assigned using our routine. The two dashed lines in (b) show the heights of the other two lower-altitude relevant peaks in the frequency distribution. Our routine assigns the boundary layer depth to the highest relevant peak. (c) The frequency distribution for cloud-top heights from (b) is shown.

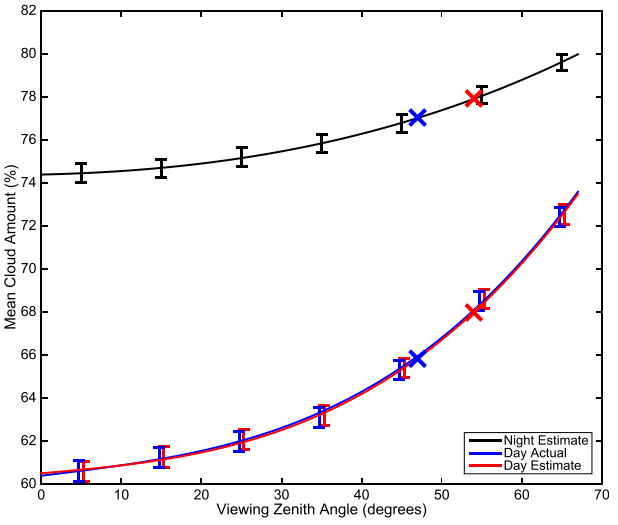

FIG. 4. The mean cloud amount and standard error for each 10° zenith angle over the regions shown in Fig. 1. Polynomial fits to the mean cloud amounts are shown as black, red, and blue curves. The red and blue × symbols show how precipitating trajectories (blue) are observed at lower zenith angles after 24 h compared to non-precipitating trajectories (red).

d. Time-evolving cloud properties

1) CLOUD COVER

Cloud cover is estimated from the cloud masks in the gridded *Aqua* MODIS level 3 (MYD08-D3) dataset (Hubanks et al. 2008; Oreopoulos 2005). Day and night cloud covers are available on a 1° × 1° latitude–longitude grid, taken approximately at 1330 and 0130 local time, respectively. A 1° × 1° grid box is included in a sample if its center falls within 100 km of a location along a trajectory at the satellite overpass time. Cloud cover is expressed in units of absolute percentage.

To sample nearly all of Earth in a single day, the MODIS sensor relies on a very wide scanning pattern, with a maximum viewing zenith angle of ~67°. Maddux et al. (2010) showed that the retrieved daytime visible cloud cover at the largest viewing zenith angle was ~14% greater than for scenes viewed at nadir because in oblique views both the sides and tops of clouds are seen. The *CloudSat* and *CALIPSO* satellite tracks are offset from the *Aqua* satellite track by ~215 km at the equator. Consequently, our initial (0 h) samples are always observed with a ~19° satellite zenith angle by MODIS, but our 12- and 24-h observations are usually viewed at considerably wider angles. If no correction were made for the change in zenith angles between 0-h and later observations, we would show, on average, an erroneous increase in cloud cover as we followed our trajectories.

Figure 4 shows how we remove the zenith angle bias. We limit this analysis just to our study regions because the zenith angle bias could look different in other regions where cloud thickness and vertical structure are different. We show separate curves for day and night. The vertical error bars are centered on the mean cloud cover and show the standard error of the mean for seven zenith angle bins. Mean cloud cover is shown for each 10° zenith angle bin (0°–10°, 10°–20°, …, 60°–67°). Curves are the polynomial fits to the means. We assume no bias when MODIS is looking straight down, so the bias at nadir is 0%, and at 67° the bias is ~5.5% at night and ~13% during the day.

Zenith angle data were available from MODIS only during daytime, requiring us to estimate the nighttime sensor zenith angle based on a grid box's distance from the satellite track. Figure 4 shows the cloud amount based on estimated (red) and actual (blue) zenith angles. The overlap of the red and blue curves shows that our estimated zenith angles match the reported angles very closely. Data for the black line (night) rely only on estimated zenith angles. The difference between the red/blue curves and the black curve shows that the zenith angle bias is markedly different between day and night because of the different MODIS cloud masks used during day and night and because nighttime cloud scenes are far more likely to be homogeneous.

All cloud-cover estimates have the zenith angle bias removed based on the sample-mean sensor zenith angle. An example of how the zenith angle bias could impact our results is shown by the red and blue × symbols on Fig. 4. Blue × symbols show the mean zenith angle at 24 h for initially precipitating trajectories while red × symbols show the mean zenith angle, also at 24 h, for nonprecipitating trajectories. The angles are different because precipitating trajectories tend to originate farther offshore and travel farther to the west, so they are sampled at a lower angle the following day. The difference between the two mean angles is 7°, overall biasing the percent cloud cover at 24 h for nonprecipitating samples high by 0.9% during the night and 2.2% during the day, both significant in the context of our results.

We use daytime cloud data from the MODIS L3 optical properties dataset to remove ice clouds and mixed-phase clouds from the analysis. The L3 dataset provides a measure of ice cloud cover, unknown cloud cover, liquid cloud cover, and single-layer liquid cloud cover. For each trajectory we use only those observations that satisfy three criteria: 1) single-layer liquid cloud cover is equal to the total liquid cloud cover, 2) the unknown cloud cover is zero, and 3) the ice cloud cover is zero. This filter is applied for all trajectories during daytime, so 24-h trajectories beginning at night are filtered once during the day, while 24-h trajectories beginning during the day are filtered at their beginning and again at their end. Sensitivity to this filter is small because of our selection of regions which have few high and midlevel clouds. Figures using filtered results are labeled accordingly.

2) Droplet concentration from MODIS optical properties

LWP and cloud droplet effective radius r_e are available for daytime only and come from the cloud optical properties product within the MODIS level 3 dataset (King et al. 2003). MODIS LWP values are for cloudy retrievals only and are not an areal average. Both LWP and r_e display zenith angle biases. For sensor zenith angles between 0° and 65°, LWP shows a bias at wide angles of $-0.01\,\mathrm{kg\,m^{-2}}$, and r_e shows a bias of 1.2 μm. The mean value of LWP is $\sim 0.085\,\mathrm{kg\,m^{-2}}$, and the mean of r_e is ~16.7 μm, for all regions and seasons combined. After removing the zenith angle biases, we use these two variables and the relationship in the following equation (Boers et al. 2006; Bennartz 2007) to estimate effective cloud droplet number concentration N_{eff} specifically for clouds in the marine PBL:

$$N_{\mathrm{eff}} = \sqrt{2}\,\frac{3}{4}\pi\rho_{\omega}\Gamma_{\mathrm{eff}}^{1/2}\frac{\mathrm{LWP}^{1/2}}{r_e(h)^3}, \tag{1}$$

where ρ_{ω} is the density of liquid water; $\Gamma_{\mathrm{eff}} = \Gamma_{\mathrm{ad}} f_{\mathrm{ad}}$, with Γ_{ad} as a measure of the adiabatic rate of increase in liquid water content with respect to height and constant f_{ad} is an estimate of the degree of adiabaticity; and h is an estimate of cloud thickness. We then calculate droplet concentration with the relationship: $N_d = N_{\mathrm{eff}}/k$, with k assumed to be 0.8 for marine stratiform clouds (Martin et al. 1994; Wood 2000).

3) LWP using AMSR-E

The Advanced Microwave Scanning Radiometer for Earth Observing System (EOS) (AMSR-E) provides separate measures of LWP for day and night (Wentz and Meissner 2004), unlike the daytime-only MODIS LWP. The AMSR-E instrument is a passive-microwave radiometer carried aboard the *Aqua* satellite along with MODIS, providing concurrent sampling of cloud cover and LWP. The AMSR-E measures brightness temperatures at 6.925, 10.65, 18.7, 23.8, 36.5, and 89.0 GHz. The instrument has a swath width of 1450 km, corresponding to a maximum viewing zenith angle of ~46°. We performed a zenith angle test for the AMSR-E LWP data in the same way as the MODIS data described above but did not find a significant zenith angle bias. AMSR-E level 3 data are averaged to match the 1° × 1° grid of the level 3 MODIS data. After averaging, our sampling routines are identical for AMSR-E and MODIS. For the AMSR-E data we use the screening process described at the end of section 2d(1) to remove cases with ice and mixed-phase clouds based on MODIS (see above), which is coincident with AMSR-E. AMSR-E LWP values are area averaged, so they include cloudy and clear pixels.

3. Methods

The goal of this Lagrangian study is to assess whether the proposed cloud-controlling variables

(lower-tropospheric stability, PBL depth, and precipitation, all described in section 2c) affect the temporal evolution of cloud properties (cloud cover, LWP, and droplet concentration, described in section 2d) relative to the climatological-mean evolution. Basically, this means we want to see which variables (sampled at trajectory beginning, hour 0) lead to anomalous cloud breakup or persistence. Since all three cloud-controlling variables are somewhat correlated we use a binning routine, described below, to isolate the effects of each variable.

To reduce biases caused by geographic, seasonal, and diurnal effects when comparing cloud evolution, we convert all evolving cloud property data to seasonal and diurnal anomalies by subtracting the mean seasonal and diurnal cloud values of the property in question. For cloud cover and LWP, for which both daytime and nighttime data are used, the seasonal-mean removal is carried out separately for daytime and nighttime data. For cloud droplet concentration, anomalies are subtracted for daytime data only. Seasonal means are estimated using all data from 2007 to 2008. Seasons are defined as December–February, March–May, June–August, and September–November.

For a given trajectory, the 24-h Lagrangian temporal change of a cloud property anomaly is given the symbol Δ. Thus, ΔCCA, ΔLWPA, and $\Delta N_d A$ refer to the Lagrangian temporal changes in cloud cover, liquid water path, and cloud droplet concentration anomalies over 24 h. To compare the effects of cloud-controlling variables on cloud temporal evolution, we first estimate the changes in cloud property anomalies at all points along each trajectory. In other words, the Δ-anomaly approach quantifies whether the cloud property evolution along a given trajectory is occurring more or less rapidly than the climatological average evolution.

Time changes for day–day evolution and night–night cloud evolution are estimated separately and then compared in order to assess any diurnal asymmetry. There is considerable spread in the magnitude of cloud property anomalies (not shown), but these are distributed around a mean value that is zero by construction.

a. *Illustrative case of cloud-cover anomalies grouped by LTS*

As an experiment, we can group trajectories according to the value of one of the cloud-controlling variables to assess whether cloud property anomalies for the trajectory subgroups evolve more or less rapidly than the climatological evolution. As an example, Fig. 5 shows distributions of CCA grouped by whether LTS at the trajectory start point is higher or lower than its climatological average at that location. Although there is considerable spread for both high- and low-LTS sets, differences are apparent. The above-mean-LTS trajectories show a somewhat tighter spread and a higher median CCA throughout the evolving 24-h trajectory (Fig. 5).

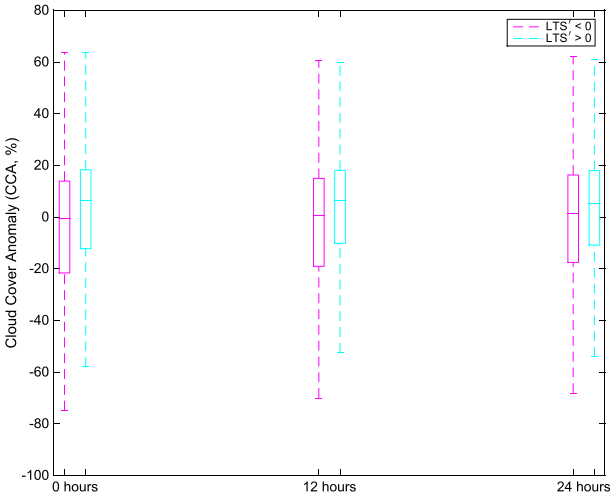

FIG. 5. Box plots showing the median CCA (middle horizontal line), 25th and 75th percentiles (box edges), and extent of the most extreme data points that are not outliers (dashed whiskers). Trajectories are separated by whether they begin with above- or below-zero LTS′.

To test whether the high- and low-LTS trajectories show statistically significant differences in mean cloud-cover anomalies, we estimate standard errors (two sigma) for all day and night CCAs at 0, 12, and 24 h for any group of trajectories assuming that any contributing trajectory is independent of the others. The two-sigma standard error bars for high and low LTS are significantly separated (Fig. 6a). This shows that initially high LTS is on average significantly associated with above normal cloudiness and vice versa, consistent with previous studies (e.g., Klein and Hartmann 1993). The mean CCA of all trajectories (shown in black in Fig. 6a) shows a slight increase over time, which we believe to be an artifact likely caused by some remaining zenith angle bias, but is sufficiently small in magnitude to have little impact on the significance of the comparison. The zenith angle bias may have an average effect of around 1.5%, while the separation between mean CCA values for high- and low-LTS subsets is closer to 3%–6%. In Fig. 6b we subtract the mean anomaly for all trajectories so we are comparing the behavior of the subsets relative to the mean of all trajectories. In the remainder of this manuscript, we perform this additional subtraction for all evolving cloud properties.

In the legend of Fig. 6b, we show the 24-h change in CCA (i.e., ΔCCA) for each subset relative to the mean

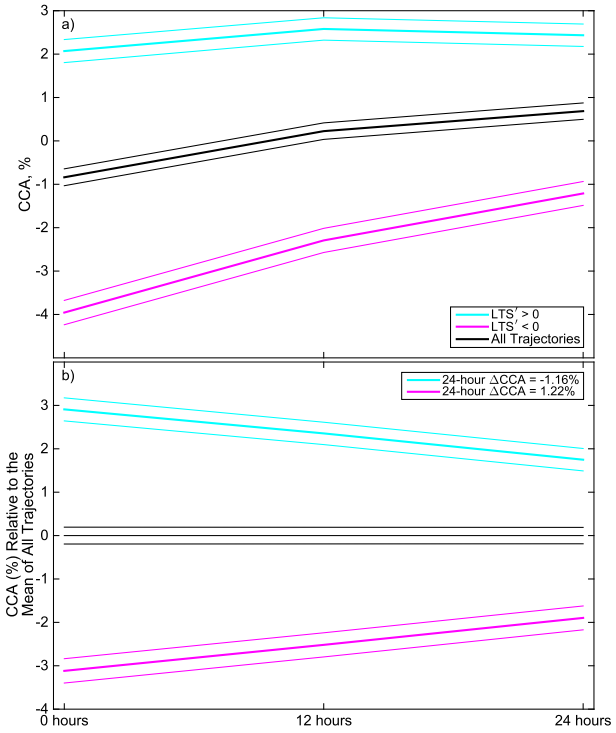

FIG. 6. (a) Mean and two-sigma standard error for CCA (%) at 0, 12, and 24 h for all trajectories, and trajectories with above- or below-zero LTS′ at 0 h. (b) As in (a), but with the mean evolution of all trajectories [black line from (a)] subtracted from all plots in (a).

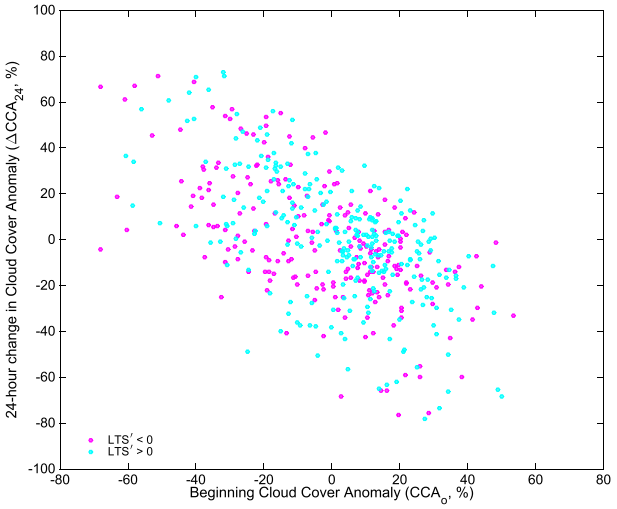

FIG. 7. A scatterplot of 24-h ΔCCA_{24} (%) vs their beginning CCA_o (%). We show a point only for every ninetieth trajectory to avoid excessive clutter.

ΔCCA for all trajectories. The numbers show a curious discrepancy with our expectations. That is, on average, ΔCCAs in more stable environments are negative and ΔCCAs in less stable environments are positive. This result is not consistent with previous findings, which tend to support the opposite conclusion—namely, that cloud cover in the less stable environment should decline relative to the more stable environment.

The above inconsistency is the result of our failure to take into account the difference in initial CCAs between the high- and low-LTS trajectory groups. Initial CCAs are significantly greater in stable environments (Fig. 6a). As a thought experiment we can consider an extreme version of this effect using two groups of trajectories: one group has only trajectories with completely clear skies (0% cloud cover) at the beginning and the other group has only overcast cases (100% cloud cover) at the beginning. Because of the bounded nature of cloud cover, each of these groups can either show no change or evolve in one direction only. The only realistic outcome, unless there is no evolution at all, is that the mean ΔCC of the two groups must evolve such that the initially clear group shows a mean increase in cloud cover and the overcast group shows a decrease. Anomalies are similarly bounded: an anomaly of −100% can only increase in time, while an anomaly of +100% can only decrease. This limitation puts bounds on how cloud cover can evolve for any starting anomaly. This is discussed further in appendix A.

Evidence of this bounding for both LTS groups is seen in scatterplots (Fig. 7), in which ΔCCA over 24 h is plotted against the beginning CCA, with trajectories color coded by whether they are high- or low-LTS trajectories. There is considerable spread in the plots, but both high- and low-LTS groups show a negative relationship with correlation coefficients r of approximately −0.62 and slopes of approximately −0.74 (both r and the slope are the same for high- and low-LTS sets). Thus, on average, positive initial CCAs tend to become less positive while negative initial CCAs tend to become less negative. The high- and low-LTS scatterplots in Fig. 7 look indistinguishable, but our samples sizes are large enough (only 1 in 90 trajectories are shown) to search for subtle but statistically significant differences between the two samples.

In Fig. 8 we show the mean and standard error of 24-h ΔCCA for six bins of beginning CCA for high- and low-LTS trajectory groups. For each group, we also show the initial mean CCA along the bottom and the corresponding mean ΔCCA at the right. For each beginning CCA bin the corresponding ΔCCA is significantly greater for the high-LTS group, now agreeing with prior observations showing that cloud cover is more persistent in stable environments. The unbinned mean ΔCCA values on the far right show exactly opposite behavior. This is because the difference in mean initial CCA for the high- and low-LTS groups is large enough to obscure

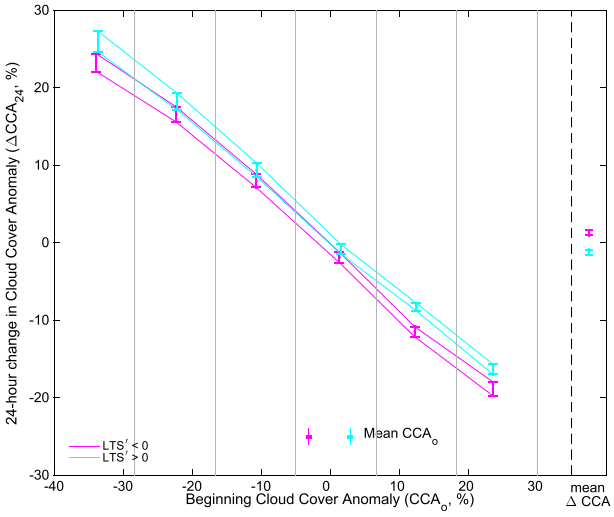

FIG. 8. Two-sigma standard error bounds around the mean 24-h ΔCCA averaged for six bins of initial CCA for trajectories with initial LTS′ above and below zero. The overall (nonbinned) mean ΔCCA for both sets is shown on the right, curiously oriented opposite to the orientations of the two lines. The overall mean initial CCA for both sets is shown along the bottom, illustrating the significant difference between the mean starting anomalies. The dashed vertical line separates the mean values from the rest of the figure, indicating that the x axis does not apply to those points, which are for all x values.

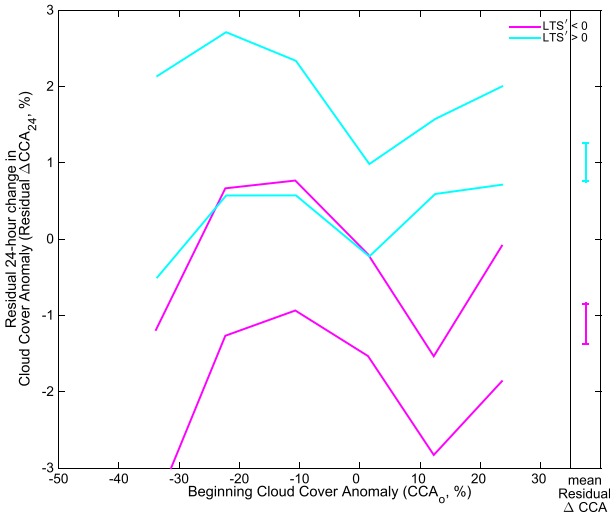

FIG. 9. Two-sigma standard error bounds around the mean residual ΔCCA for the same six bins and trajectory groups as in Fig. 8. Residual values are based on the plots in Fig. 8 with the average linear dependence on initial CCA removed. On the far right we show the two-sigma standard error bounds for the mean residual ΔCCA for all bins for both sets of trajectories. Significant separation between overall means is apparent, and this time the orientation agrees with that of the two plots.

the actual signal given the negative CCA–ΔCCA relationship.

The true difference between ΔCCA for high- and low-LTS groups is shown by the separation between the high- and low-LTS confidence intervals in Fig. 8. To better display this difference, we perform a robust linear regression to remove the slope from both samples, with the resulting Fig. 9 showing the differences once the linear trend is removed. Slopes are estimated separately for the high- and low-LTS lines, one slope estimate per high or low set. We can now compare the mean residual ΔCCA values between the high- and low-LTS groups for all bins (far right of Fig. 9), where the separation between those values reflects the mean vertical separation between the high- and low-LTS sets in Fig. 8.

The lines in Fig. 8 show that on average the 24-h ΔCCA results in a partial reduction of the initial anomaly. The same behavior is found for the other evolving variables (not shown). The rate at which anomalies decay is discussed at length in appendix A. If the means of the residual Δ-anomaly values (e.g., Δ cloud-cover anomaly, ΔLWP anomaly, or ΔN_d anomaly) for different trajectory groups (e.g., groupings conditioned on values of cloud-controlling variables) are shown to be significantly distinct using this method, we will conclude that the groups evolve differently and that the cloud-controlling variable is a useful determinant of the magnitude of the cloud evolution. In appendix B, we show that alternative methods exist to achieve quantitatively similar results.

b. *Untangling correlations between cloud-controlling variables*

A potential source of indeterminacy in this study is the correlation between cloud-controlling variables. All three of our variables are correlated with one another to some extent. Precipitation rate and frequency correlate positively with PBL depth while precipitation rate correlates negatively with LTS anomalies. PBL depth correlates negatively with LTS anomalies. This is problematic because we want to assess whether these variables individually affect ΔCCA. To separate the effects of variables, we introduce a binning routine comparing residual ΔCCA for two groups of trajectories within bins of a constant second controlling variable to remove the confounding effect of the second variable.

The positive correlation between PBL depth and precipitation shows why this binning is necessary. Precipitation is more common in deep PBLs and without taking that into account we could draw the erroneous conclusion that precipitation is causing Sc breakup when the real cause may be decoupling due to a deeper PBL. This binning routine will allow us to look at the effect of precipitation with PBL depth held relatively constant.

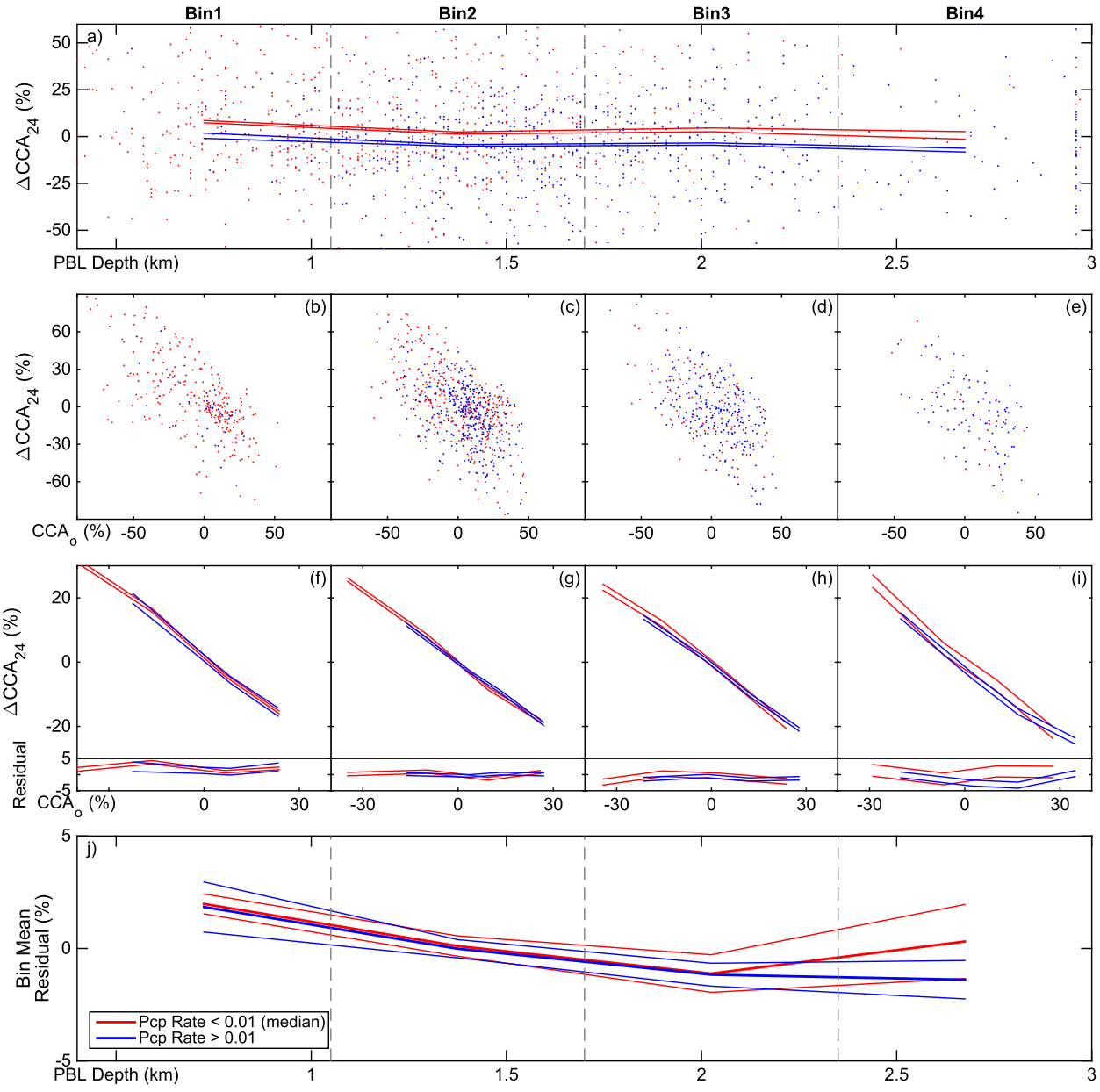

FIG. 10. (a) 24-h ΔCCA values plotted as a function of their initial PBL depth for two sets of trajectories. Sets are separated by whether they have above- or below-median rain rates at hour 0. We show only every thirtieth value to avoid clutter. The mean and two-sigma standard error ΔCCA for each bin of initial PBL depth is also shown. (b)–(e) 24-h ΔCCA values plotted against their 0-h values within each PBL depth bin (1–4, respectively) for each set of trajectories. (f)–(i) The mean ΔCCA for four subbins of initial CCA within the four bins of initial PBL depth (1–4, respectively). Linear fits were applied to each plot individually, and the slopes were removed to produce the residuals at the bottom of each frame. (j) The average of each set of residuals within each PBL depth bin is shown. The mean residual ΔCCA for each bin of PBL depth for each set of trajectories with two-sigma standard error bounds also shown. The significant separation seen in (a) is entirely gone when we account for the relationship between ΔCCA and initial CCA.

Trajectories are separated into two groups—above- and below-median initial precipitation rate—and we then plot ΔCCA values for four bins of PBL depth (Fig. 10a). The two lines in Fig. 10a show significant separation in mean ΔCCA for the two sets across all four PBL depth bins but the different initial CCA distributions for the two trajectory groups have not been accounted for. Figures 10b–e show ΔCCA as a function of initial CCA for both sets of trajectories within each bin of PBL depth, similar to Fig. 7. Figures 10f–i show the mean

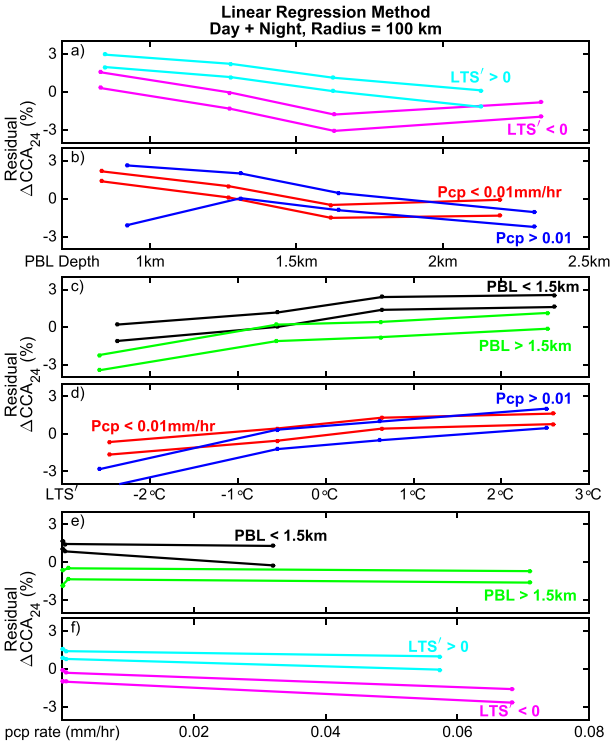

FIG. 11. (a),(b) Residual 24-h ΔCCA for bins of constant boundary layer depth, (c),(d) LTS′, and (e),(f) rain rate. Trajectories are broken into two sets for each plot, with high (>0) and low (<0) LTS′ in (a) and (f), above- and below-median (~0.01 mm h^{-1}) rain rates in (b) and (d), and shallow (<1.5 km) vs deep (>1.5 km) boundary layers in (c) and (e). Lines are the two-sigma standard error bounds for each mean value. Bins are not uniform but are instead chosen to have equal numbers of trajectories per bin, with 25% of all trajectories in each bin. Dots indicate bin centers.

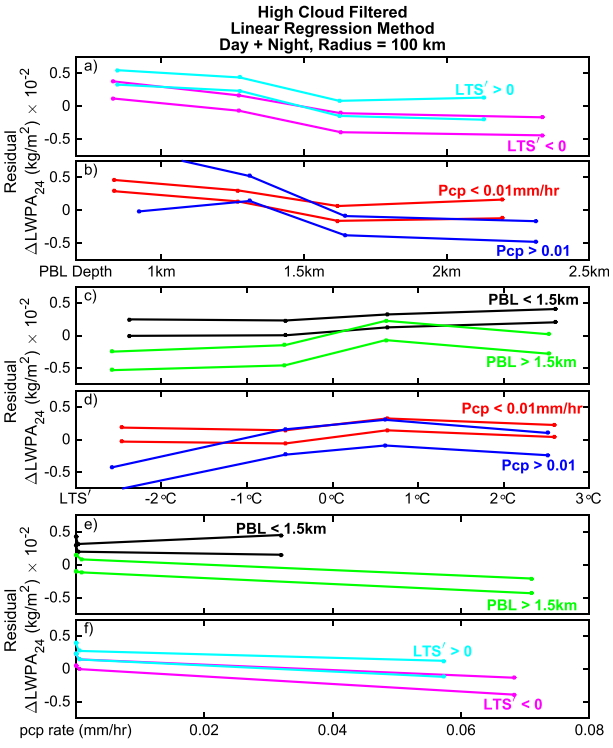

FIG. 12. As in Fig. 11, but for residual 24-h ΔLWPA. We use only observations with no high or middle clouds and no multilayer clouds.

ΔCCA for initial CCA bins, with Fig. 10j showing the mean residuals per PBL bin after the slope between ΔCCA and initial CCA has been removed (as in Figs. 8 and 9, respectively). Slopes are fitted separately for each subset within each PBL depth bin. The lack of significant separation between the two groups shows that precipitation is a less significant factor in Sc breakup when the initial distribution and PBL depth are taken into consideration. We have also calculated our results using slopes fit to all available data points, not just the subsets within bins, producing virtually identical results. This indicates that the ΔCCA versus CCA slope is, on average, consistent across all subsets.

Results for this paper use this approach throughout, but to conserve space we only show the equivalent of Fig. 10j in subsequent plots. We alter the binning routine to keep the number of trajectories per controlling variable bin constant rather than requiring bin boundaries to be evenly spaced as in Fig. 10. In appendix B we show two other routines that produce quantitatively similar results to our linear regression method.

Here, we limit our analysis to the effects of LTS, PBL depth, and precipitation rate on cloud evolution. We choose these three because each has been identified from previous studies as being potentially important for cloud evolution. Stronger LTS leads to less cloud-top entrainment, whereas deeper PBLs tend to be decoupled leading to altered moisture and aerosol sources, and precipitation drives changes to the thermodynamic structure in the PBL and can remove aerosols and impact cloud droplet concentration. We do not suggest that the three controlling variables being evaluated here are exhaustive, and future study will explore others.

4. Results

Trajectories are separated into groups determined by whether the initial values of LTS, PBL depth, or precipitation rate are high or low. Confidence intervals of residual values of ΔCCA (Fig. 11), ΔLWPA (Fig. 12), and $\Delta N_d A$ (Fig. 13) for the two groups are shown as a function of a second controlling variable along the abscissa. Bins are not uniform, but are instead chosen to have equal numbers of trajectories per bin (four bins, each with 25% of the trajectories). Below, we discuss each figure in turn.

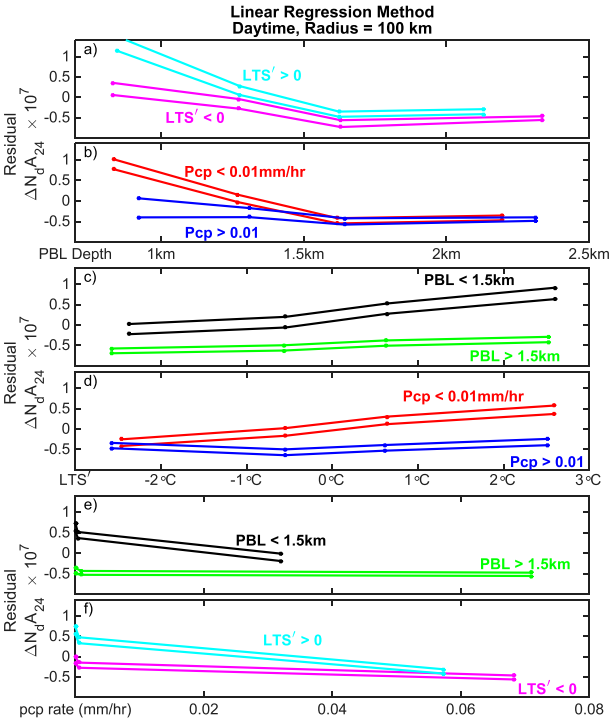

FIG. 13. As in Fig. 11, but for residual 24-h $\Delta N_d A$.

a. Δ *cloud-cover anomalies*

The strong dependence of ΔCCA on PBL depth is clear, and for a given PBL depth, cloud cover is also more persistent when LTS is strong (Fig. 11a). This implies that positive LTS anomalies significantly suppress cloud breakup until PBL depth exceeds 2 km, where the LTS effect appears less significant. Figure 11b suggests that the effects of precipitation are not nearly as strong as LTS when PBL depth is accounted for. At best the evidence suggests that higher rain rates in deeper PBLs may lead to marginally more rapid cloud breakup. The offset along the abscissa of the two groups in Fig. 11b indicates that precipitation tends to be more frequent in deeper PBLs, which is consistent with previous findings (e.g., Bretherton et al. 2010; Wood 2012). Without controlling for PBL depth, precipitation could falsely appear to be a major contributing factor in Sc breakup.

Residual ΔCCA for bins of constant LTS anomalies are shown in Figs. 11c and 11d. Both plots show a positive slope, confirming that LTS is a significant factor in cloud breakup, with positive LTS anomalies associated with more persistent clouds. Figure 11c shows that PBL depth is an independent factor in cloud breakup when LTS is held constant. Figure 11d shows little separation for above- and below-median precipitation, especially when LTS is high, once again suggesting that precipitation is less of a factor in cloud-cover evolution compared to PBL depth and LTS. The measure of precipitation used here is but one metric, however, and in section 4e we will investigate other metrics.

Figures 11e and 11f show residual ΔCCA for bins of constant precipitation rate. This result verifies the findings in the other panels, namely that LTS and PBL depth are more significant factors in cloud breakup compared with precipitation, and that clouds persist in shallow PBLs and in environments with high LTS. Three of the four slopes in Figs. 11e and 11f are negative, possibly indicating that heavier precipitation rates may slightly favor cloud breakup, but these slopes are not as strong as the slopes in Figs. 11a–d. We investigate this further in section 4e.

b. ΔLWP *anomalies*

Figure 12 follows the same template as Fig. 11, but for ΔLWPA. The evolution of areal-mean LWP behaves only slightly differently than the evolution of cloud cover in terms of sensitivity to controlling variables. LTS anomalies show only weakly significant effect on ΔLWPA evolution within bins of constant PBL depth, with overlap seen between error bounds (Fig. 12a). The relationship between LTS anomalies (LTS′) and ΔLWPA agrees with the relationship between LTS′ and ΔCCA, with high LTS associated with more cloud and with marginally more LWP. Precipitation shows a somewhat stronger relationship with LWP than with cloud cover (Figs. 12b,d). Rain may lead to a relative reduction in LWP in deeper PBLs (Fig. 12b). PBL depth has a similar effect on LWP as on cloud cover, with a tendency for increased LWP in shallow PBLs (Figs. 12c,e). The increasing LWP anomalies in shallow PBLs are very likely due to the boundary layer deepening over time, while the decrease in LWP for deep PBLs likely is due to the cloud breakup.

c. ΔN_d *anomalies*

Figure 13 again follows the template of Figs. 11 and 12, but for residual ΔN_d anomalies ($\Delta N_d A$). Since N_d declines climatologically as trajectories advect offshore, most positive residual ΔN_d anomalies are showing trajectories where N_d fails to decline, meaning an environment of persistent droplet concentration. The evolution of N_d is strongly dependent on PBL depth for PBLs shallower than 1.5 km (Figs. 13a,b). In shallow PBLs, N_d is generally more persistent, but is also dependent on LTS and precipitation, with higher stability and less precipitation associated with persisting N_d anomalies. The evolution of N_d in deeper PBLs is not significantly affected by LTS or precipitation, and N_d shows consistent relative declines in PBLs deeper than

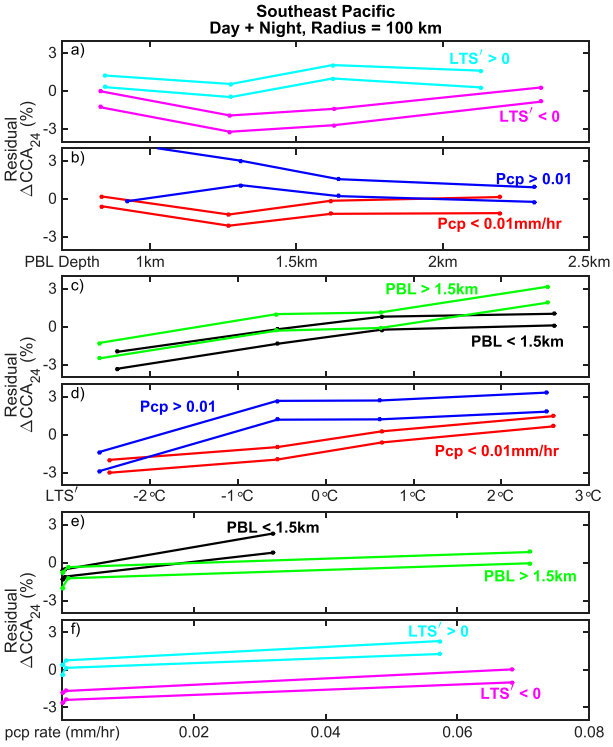

FIG. 14. As in Fig. 11, but for residual 24-h ΔCCA for the southeast Pacific region only.

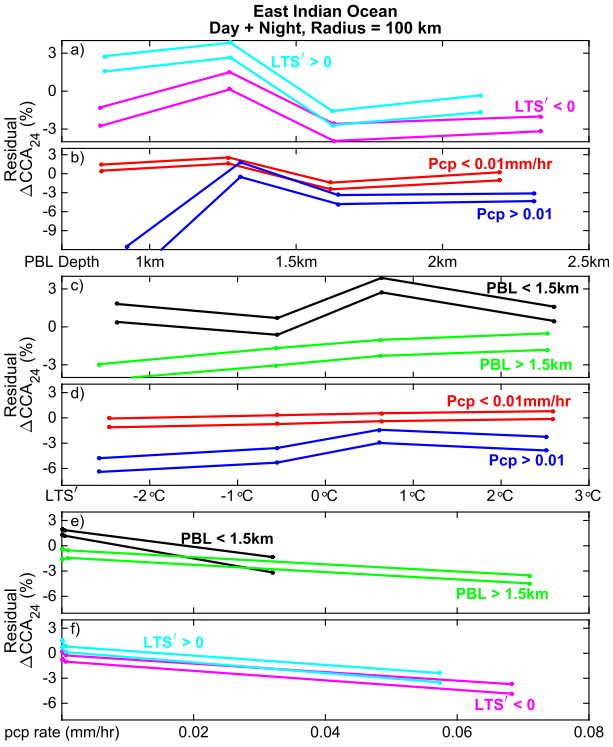

FIG. 15. As in Fig. 11, but for residual 24-h ΔCCA for the east Indian Ocean only.

1.5 km (Figs. 13a,b). This is reinforced by Figs. 13c,e, which both show consistent, slightly negative residual $\Delta N_d A$ in deep PBLs, but positive relative changes in shallow PBLs. Slopes of the shallow PBL plots (black curves in Figs. 13c,e) agree with our interpretation that rain and low LTS both lead to relative declines in N_d, as long as the PBL is shallow.

d. *Regional differences*

We have carried out the ΔCCA analysis described in the prior three subsections for each of our regions (Fig. 1) individually. We choose two of our regions—the southeastern Pacific (Fig. 14) and the eastern Indian Ocean (Fig. 15)—because they exhibit somewhat different behavior relative to the all-region aggregates shown in Fig. 11.

Figure 14a shows agreement with our prior results: low LTS is associated with cloud breakup. The precipitation rate breakdown (Fig. 14b) shows a distinctly different relationship for this region: clouds may persist with increased precipitation, especially in shallower PBLs, though the sample size is small and significance becomes marginal. Figures 14c and 14d show trajectories grouped by PBL depth and above- and below-median rain rate, respectively, for bins of constant LTS anomaly. An initial view of the relationship in Fig. 14c suggests that PBL depth may have an opposite effect on ΔCCA over the southeastern Pacific relative to the all-region mean. However, that relationship is likely muddied by the inverse relationship between precipitation and ΔCCA. Figure 14e shows that PBL depth has little effect on ΔCCA when there is very weak or no precipitation but that deep PBLs still tend to break up more readily when rain rate is positive and held constant. Figure 14d again shows that higher rain rates over the southeast Pacific lead to cloud persistence.

Figure 15 shows that rain appears to contribute more strongly to cloud breakup in the eastern Indian Ocean than in other regions, and PBL depth may have a stronger contribution to cloud breakup compared to LTS, which differs from the order shown for all regions, though the strength of the relationship in Fig. 15c may be buoyed by the stronger precipitation effect. Figures 15e and 15f show a pronounced negative slope for all plots, again showing that increased rain rate appears to be associated with Sc breakup in the southeast Indian Ocean.

We do not show regional breakdowns for LWP and N_d. Liquid water path does not show consistently significant results when broken down by region. LWP shows the widest error bars and least separation between sets (e.g., Fig. 12) and this is exacerbated with

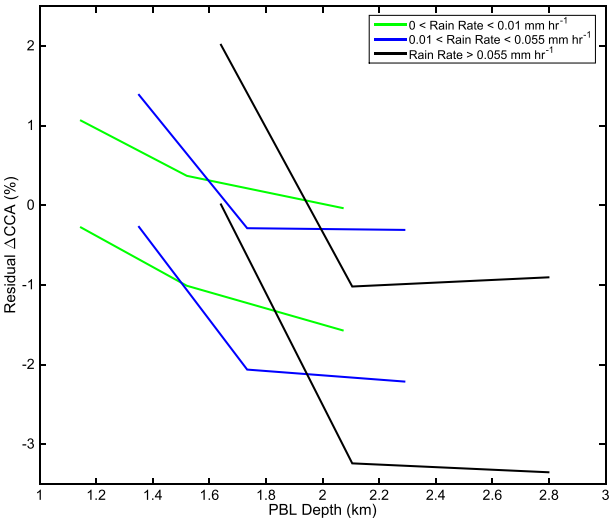

FIG. 16. Residual ΔCCA for bins of constant PBL depth. Trajectories are divided into three groups based on the sample-mean rain rate at the beginning of the trajectory: below-median rain rate (green), "moderate" rain rate (blue), and "heavy" rain rate (black). Lines show the standard two-sigma standard error bounds of the mean residual ΔCCA. Bins are not uniform but are instead chosen to have equal numbers of trajectories per bin, with 33% of the trajectories from each group in each bin.

smaller sample sizes for a regional breakdown. This abundance of error is mostly due to the high cloud filter. Results for N_d evolution for each region are much more consistent, with all of the aforementioned relationships remaining intact even when broken down by region.

e. *Sensitivity to aspects of precipitation*

There are different aspects of precipitation that might influence PBLs in different ways. For example, Wang and Feingold (2009) find that heavy precipitation reaching the surface is what causes a transition from closed to open cells. Further, Terai et al. (2014) find similar cloud base precipitation rates inside and outside POCs on average, but markedly higher rates in open cells at the surface. We explore this further in Fig. 16, which excludes any nonprecipitating trajectories, and shows residual ΔCCA against PBL depth for three trajectory groups with low, moderate, and heavy precipitation rate. These results suggest that precipitation is associated with cloud persistence in shallow PBLs but with breakup in deeper PBLs provided the rain rate is high enough. Trajectories starting with low rain rates (green) show a lower slope than for trajectories starting with moderate and heavy rain rates (blue and black). Increasing the rain rate appears to lead to a steeper negative slope, which means that heavier rain in a shallow PBL leads to more cloud persistence while heavier rain in a deeper PBL leads to more rapid cloud decreases. It is possible that the heavier rain in persistently cloudy shallow PBLs is a symptom of a stronger overturning circulation, acting to sustain the cloud deck and drive stronger precipitation. For deeper PBLs it is possible that high rain rates simply act to remove liquid from decoupled stratocumulus decks, leading to faster breakup because the cloud deck is partially cut off from its moisture source.

A diurnal breakdown (not shown) indicates that the relationships shown in Fig. 16 are predominantly nocturnal, and during the day the different rain-rate curves are not statistically significant from one another. Despite a lack of statistical significance, the general trend of heavier precipitation acting to break up clouds regardless of PBL depth is observed during daytime. The majority of precipitating trajectories begin at night, so this effect could be real, or could be due to insufficient daytime observations. If real, it is possibly because nighttime PBLs are more strongly coupled than daytime PBLs owing to the stronger radiatively driven circulation at night. The shallower PBLs seen on the left side of Fig. 16 may represent well-mixed PBLs at night, but the majority of them may become stratified or decoupled during the day, leading to the observed difference in precipitation effects.

We examined a simpler version of Fig. 16 for each region (not shown), with trajectories grouped by above- or below-median rain rate. All regions show the same pattern of negative slopes seen in Fig. 16, again with the heavy-rain-rate group showing a more negative slope in each region. Once again, this suggests that a higher rain rate may lead to more persistence in shallow PBLs but may cause breakup in deeper PBLs.

5. Discussion

In this work, we have examined cloud temporal evolution as a function of several different potentially cloud-controlling variables. In doing so, we were forced to make a number of decisions regarding trajectory duration, sampling radius around trajectory points, choice of controlling variable bins, etc. We have reproduced many of our results with different choices to ascertain the robustness of our findings.

First, we explored using sampling radii of 100, 200, 400, 800, and 1600 km. A radius smaller than 100 km is not suitable owing to possible errors in the wind fields that generate trajectories. A typical trajectory travels about 600 km in a day (average speed of 6.9 m s^{-1}). A pessimistic error estimate in wind speed of 1 m s^{-1} translates to a possible position discrepancy of ~170 km in a day. To ensure that we sample at least some of the same clouds at 0 and 24 h, we need a sampling radius

exceeding 85 km. Hence, in this work we used 100 km. Repeating our analysis using larger sampling radii, the results remain qualitatively unchanged, although statistical significance improves.

We chose also to show results only for 24-h changes in order to observe a complete diurnal cycle. We examined separately trajectories restricted to day–day or night–night evolution to test for asymmetries. When we restricted our analysis this way, the results were qualitatively unchanged for Figs. 11–13. The only diurnal effect of note was for precipitation rate as discussed above in section 4e.

Thresholds were also chosen to group trajectories by values of PBL depth and precipitation rate. Our threshold values reflect a compromise between a need to separate variables by their physical effects but also keep numbers comparable between sets of trajectories. Across all trajectories median and mean PBL depth are 1.45 and 1.50 km, respectively. We do not use anomalies for PBL depth because the degree of decoupling is related to the absolute PBL depth (Wood and Bretherton 2004). Several threshold values were tested between 1 and 1.5 km, with 1 km being closer to the depth where decoupling begins to be observed (Wood and Bretherton 2004). For any threshold between 1 and 1.5 km, our PBL depth results were qualitatively identical; we choose the high value of 1.5 km to keep the number of trajectories even between groups. PBL depth does show a diurnal cycle but this is small compared with the range of depths across the entire trajectory set. We took a similar approach for rain rate.

6. Conclusions

In this work, we describe a method to quantify the time evolution of low-cloud properties (cloud cover, LWP, and cloud droplet concentration) along Lagrangian boundary layer trajectories and explore the impact of several potentially cloud-controlling variables on this evolution. Biases caused by seasonal and geographic effects are reduced by using seasonal, location-specific anomalies for all three cloud properties. Satellite (viewing) zenith angle biases are identified and removed. Cloud property changes are examined over 24 h. Most importantly, we show that the average time change in cloud properties is strongly related to the initial cloud amount, consistent with anomalies evolving as autocorrelative red noise processes. We show that it is necessary to derive a residual Δ-anomaly variable that allows us to more directly compare cloud evolution in groups of trajectories with differing initial cloud property values. The linear relationship between initial values of the anomalies and their time changes will be explored further in future work to examine decorrelation time scales for low-cloud fields.

Low-cloud evolution is modulated by several factors. Changes in cloud cover (and likely albedo) appear to be affected more by PBL depth and lower-tropospheric stability than by precipitation. Clouds in deeper PBLs and in less stable environments appear to break up more readily than clouds in shallow PBLs or stable environments. The result that clouds in deeper PBLs tend to break up more quickly, although expected from our basic theory of decoupling and breakup (Bretherton and Wyant 1997), has not been shown previously in a Lagrangian study. Mauger and Norris (2010) do show this using a reasonable proxy for PBL decoupling but suggested that future studies use the CALIOP data as we have done. Burleyson and Yuter (2015) use SST as a PBL depth proxy and show a faster reduction in cloud cover during the early to late morning decline in cloud cover in deep PBLs. Here we show the PBL depth impact using a more direct measure of PBL depth, and we show that the PBL effect acts independently of precipitation and LTS. The result that lower LTS leads to cloud breakup agrees with Sandu et al. (2010) and Mauger and Norris (2010).

We propose a few physical processes associated with our results. Strong inversions may inhibit cloud-top entrainment of dry air, allowing cloud cover to persist. Moisture and aerosol transport into the cloud layer may be limited in deep, decoupled PBLs, while strong Cu updrafts into decoupled Sc decks may enhance entrainment and disrupt the thermodynamically driven circulation leading to cloud breakup. There are regional preferences as to which cloud-controlling factor is more strongly associated with cloud-cover evolution, which warrant further attention.

The effect of precipitation on cloud evolution appears complex. Further modeling studies focusing on precipitation intensity are needed. Figure 16 shows that rain may lead to an amplification of the observed PBL depth impact. We show increasingly heavy precipitation is associated with cloud persistence in shallower PBLs and with cloud reduction in deeper PBLs.

A regional comparison of trajectories with above- and below-median precipitation showed little consistency when PBL depth was accounted for: rain showed little significant effect in the northeast Pacific and southeast Atlantic. Rain is associated with cloud persistence in the southeast Pacific but with cloud breakup in the east Indian Ocean. Observation numbers were not sufficient to thoroughly examine the effects of heavy precipitation regionally, though a cursory look produced evidence supporting our conclusion that precipitation exacerbates the effects of PBL depth in all regions. Future

work will focus on determining what environmental factors modulate the effects of rain on cloud evolution, most notably PBL depth, and why and how the relationships vary regionally.

Precipitation is shown to affect LWP and N_d, leading to a relative decline in both. The explanation may be as simple as the physical removal of liquid water and aerosol (Albrecht 1989; Wood et al. 2012) from the cloud layer. The decline in N_d related to precipitation is seen only when the PBL is shallow; N_d appears to be affected by very little in deeper PBLs where it shows a consistent relative decline. This may be because the cloud layer in a deeper decoupled PBL is partially cut off from the aerosol source at the sea surface. Future work may focus on estimating entrainment for each trajectory using estimates of PBL depth from MODIS (e.g., Wood and Bretherton 2004).

Results from this work support existing hypotheses about stratocumulus evolution (e.g., decoupled PBLs tend to break up, weaker inversions are associated with Sc breakup, and that precipitation rate plays a more complex, but important, role in Sc evolution) while inviting further research with a larger sample size. We hope to further apply our approach to a larger set of cloud-controlling variables to study the proposed mechanisms for cloud breakup at varying time scales and to attempt to quantify the radiative and climatological effects. The Lagrangian technique developed here can also be used to evaluate the accuracy of the representation of the time evolution of clouds in large-scale models.

Acknowledgments. This work was supported by NASA Grant NNXBAQ35G (*CloudSat* and *CALIPSO* science team). Productive collaboration and discussion was provided by Sandra Yuter, Casey Burleyson, Christopher Bretherton, Christopher Terai, Johannes Mohrmann, Irina Sandu, and Stephen Warren. Rhea George provided valuable trajectory software. Three anonymous reviewers provided thorough and invaluable feedback.

APPENDIX A

The Linear Relationship between CCA and ΔCCA

The aim of this study is to quantify and compare how cloud properties change along thousands of unique trajectories and to see which independent cloud-controlling variables are associated with cloud property changes. In section 3, we explain why it is necessary to use seasonal/diurnal anomalies and we briefly discuss how the temporal change in cloud-cover anomaly ΔCCA along a trajectory depends on the initial value of the CCA. Here, we further explore the relationship between ΔCCA and initial CCA given the bounded nature of the CCA distribution.

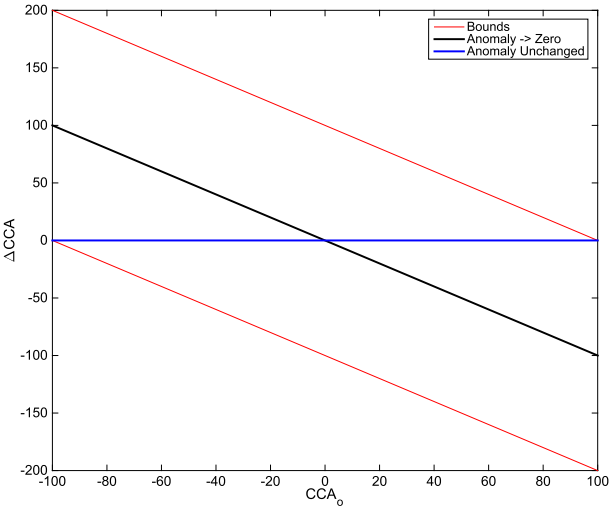

FIG. A1. The possible bounds placed on ΔCCA as a function of initial CCA. The red line shows the extreme possibilities, while the blue line shows what the relationship would look like with no change, and the black line shows what the relationship would look like if anomalies returned to 0.

A −100% anomaly represents an observation that shows no cloud cover even though it is climatologically always overcast at that point. A +100% anomaly represents a perpetually cloud-free box that happens to be completely overcast upon observation. A trajectory showing an initial −100% anomaly could (this is not likely) completely fill in with cloud cover while advecting to a climatologically clear region, thus showing a +200% ΔCCA. Figure A1 shows the possible bounds for ΔCCA given any initial CCA. The bounds are shown in red. In black we show what the ΔCCA would look like if every CCA returned to a 0% anomaly (climatology), while the flat blue line shows what the plot would look like if anomalies persisted with no change.

Most stable stochastic physical systems tend to return to their mean state, such that departures from mean behavior (i.e., anomalies) tend to decay over time. Given these practical bounds we expect to see a negative slope when plotting mean 24-h ΔCCA as a function of initial CCA, and that this slope must fall between the blue and black lines in Fig. A1. We expect that slopes of mean ΔCCA versus CCA for shorter (longer) evolution times will lie nearer the blue (black) line. Indeed, Fig. A2 shows that this is the case for trajectory evolution times of 12, 24, 36, and 48 h. The black line in this case represents an experiment where we randomize trajectory start and end points, indicating behavior

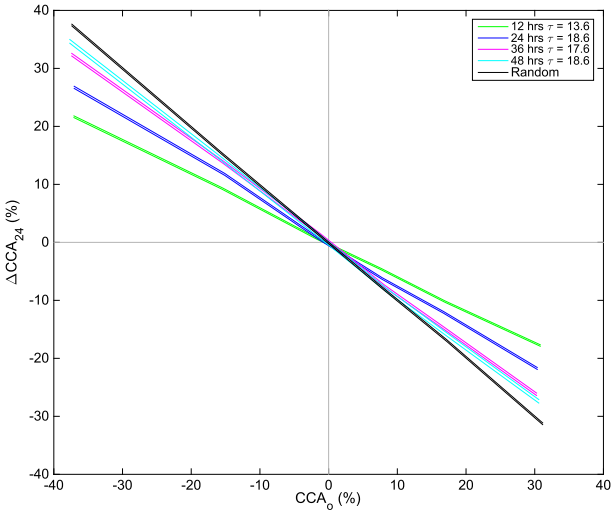

FIG. A2. Mean 24-h ΔCCA for bins of initial CCA for trajectories of duration 12, 24, 36, and 48 h. Two-sigma standard error bounds surrounding each mean value are shown. Also shown is an example where we randomly matched CCAs at each end point to the CCAs at each starting point and calculated ΔCCA. The black line rests exactly on a −1:1 line. Here, τ is the *e*-folding time for an anomaly, defined in (A1).

without any persistence (i.e., where anomalies decay instantaneously). The other lines show that mean ΔCCA displays an inverse linear dependence upon initial CCA out to 48 h. The lesser slope of the green (12 h) line tells us that anomalies are more persistent at 12 h than at 48 h, as expected for a stochastic process with a particular time scale. At 48 h, mean ΔCCAs are nearly equivalent to those for randomized end points indicating near-complete decay of the initial anomalies.

Figure A2 illustrates why we need to be cognizant of the initial anomaly: on average, ΔCCAs along trajectories tend to act to return initial anomalies to the mean state (an anomaly of zero). Any comparison of ΔCCA for different values of a controlling variable must take this into account; otherwise, the comparison is biased by the almost inevitably uneven distribution of initial CCAs between two groups.

The rate at which the CCAs decay is quantifiable using the slope of each line in Fig. A2 along with an assumption of a red noise process to estimate the *e*-folding (decay) time τ of CC anomalies along our trajectories. For a red noise process, the lagged autocorrelation $r(T)$ of CCA(t) with CCA($t + T$) at lag time T is

$$r(T) = e^{-T/\tau}. \tag{A1}$$

An autocorrelation can be expressed as a covariance

$$r(T) = \mathrm{Cov}[\mathrm{CCA}(t), \mathrm{CCA}(t+T)]/\mathrm{Var}[\mathrm{CCA}(t)]. \tag{A2}$$

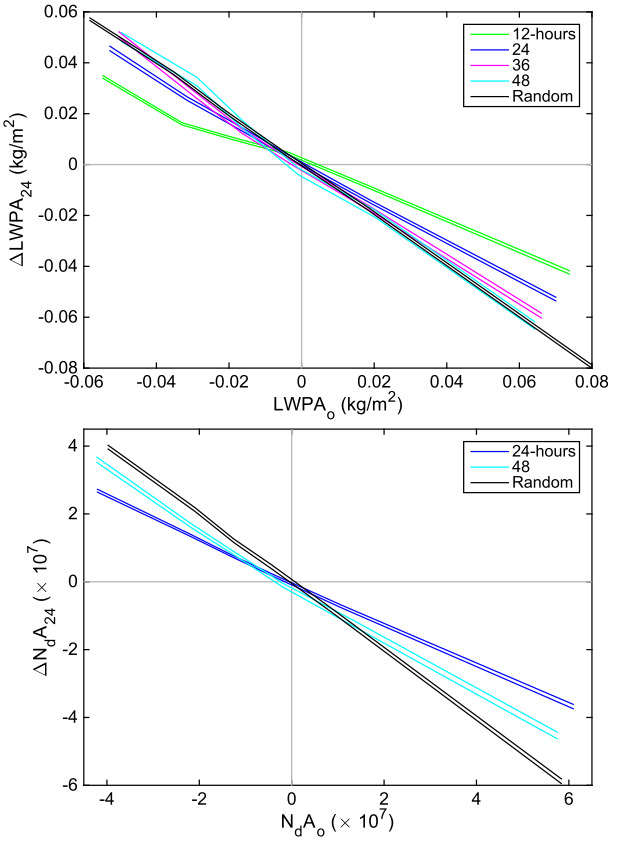

FIG. A3. Mean 24-h (top) ΔLWPA and (bottom) $\Delta N_d A$ for bins of their initial anomalies for trajectories of duration 12, 24, 36, and 48 h. Two-sigma standard error bounds surrounding each mean value are shown. Also shown is an example where we randomly matched anomalies at each end point to the anomalies at each starting point and calculated ΔLWP and $\Delta N_d A$. The black line rests exactly on a −1:1 line.

Noting that the slope of a linear fit between two variables, x and y can be written as

$$b = \mathrm{Cov}(x, y)/\mathrm{Var}(x). \tag{A3}$$

Substituting $x = \mathrm{CCA}(t)$ and $y = \mathrm{CCA}(t + T)$ in (A3), we note from a comparison of (A2) and (A3) that the slope of the relationship between CCA(t) and CCA($t + T$) is equal to $r(t)$. Thus, from (A1) the slope of the linear relationship between $\overline{\mathrm{CCA}(t+T)}$ for binned values of $\overline{\mathrm{CCA}(t)}$ can be used to estimate the *e*-folding time τ for any lag time T. In Fig. A2, we show the mean time change in CCA [i.e., $\overline{\mathrm{CCA}(t+T) - \mathrm{CCA}(t)}$] rather than $\overline{\mathrm{CCA}(t+T)}$ for different bins of CCA(t). Thus, the slope of the relationship in Fig. A2 is equal to $r(T) - 1$. Figure A2 shows in the legend the estimated values of τ for different trajectory lag times from 12 to 48 h. For lag times from 24 to 48 h, τ estimates are all in the range 17–18 h, consistent with a red noise process being an

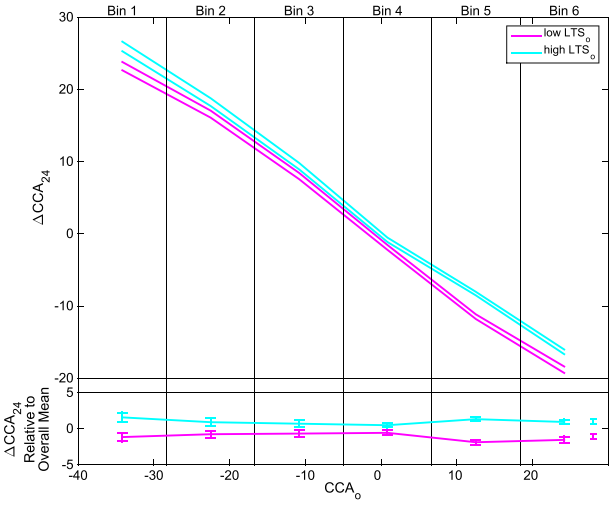

FIG. B1. (top) One-sigma standard error bounds for average 24-h ΔCCA for six bins of initial CCA. Trajectories are separated by above- or below-mean LTS′ at 0 h. (bottom) The bin-mean and standard error ΔCCA for each set of trajectories relative to the mean of all trajectories within each bin. The mean value across all bins for each set of trajectories is shown on the far right, indicating significant separation between the sets.

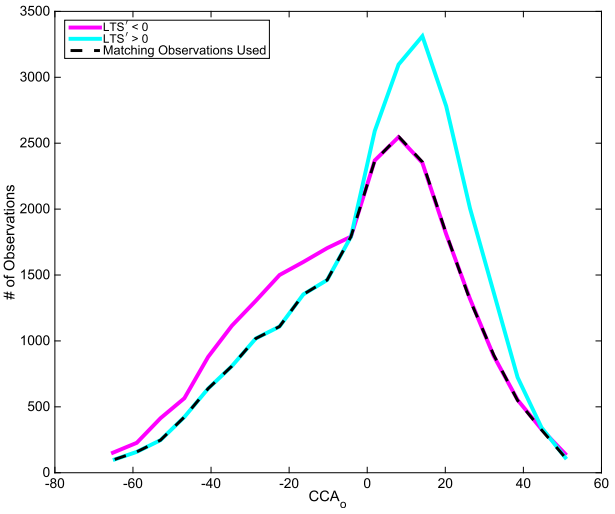

FIG. B2. A frequency distribution over 20 bins showing the number of times initial CCA values were observed for trajectories with above- and below-mean LTS′. The dashed black line shows the matched initial distributions used in our even sampling routine.

effective descriptor of cloud-cover anomaly time changes. The shorter τ for $T = 12$ h lag suggests a departure from red noise on subdaily time scales, but we do not explore this further here. We also find that τ estimates are sensitive to the sampling radius, with larger-radius samples showing significantly longer τ. We plan to explore this dependency in future analysis.

Analogous linear relationships between starting values of LWP and N_d anomalies and their mean changes are found (Fig. A3). Although LWP and N_d are not bounded in the same way that CCAs are, we nevertheless find linear, negative relationships between their starting anomalies and their mean observed changes at lags from 12 to 48 h. Correlation coefficients between initial anomalies and 24-h changes for each variable are −0.59 for CC anomalies, −0.54 for LWP anomalies, and −0.58 for N_d anomalies. Given how linear both 24-h plots appear (Fig. A3), we feel comfortable using our linear regression method for changes in LWP and N_d anomalies.

APPENDIX B

Alternative Methods to the Linear Regression from Section 3

In section 3 and appendix A we show that there is a consistent linear relationship between the mean observed time change in a variable (cloud cover, LWP, or N_d) and its initial anomaly. Anomalies on average tend to return to their mean state (anomaly = 0) over time, with larger initial anomalies undergoing typically larger changes for a given *e*-folding (damping) time scale. Sets of trajectories with different distributions of initial anomalies can be compared only when this stochastic behavior is taken into account. In section 3 we use a linear regression to achieve this by representing the mean behavior for an initial anomaly as a linear function of that anomaly, then subtracting that mean behavior to leave a residual that is no longer dependent upon the initial anomaly. These residuals can then be compared for groups of trajectories conditioned on one of the cloud-controlling variables.

The assumption of linearity in the relationships between initial anomalies and their time change is not strictly necessary, and other methods exist to account for the stochastic nature of anomalies. One option (termed here the "binning method") is by comparing the difference between mean changes in our variables within bins of starting anomalies (Fig. B1), where we show the mean ΔCCA values for bins of starting CCA values as well as the bin boundaries for trajectories with above- and below-median initial LTS anomalies. We show the average ΔCCA across all six bins on the bottom right of Fig. B1. The difference between the two subsets is nearly identical to that shown in Fig. 9, showing that the methods produce equivalent results for our LTS test example and that the assumption of linearity is not required.

Another proposed method involves subsampling our trajectories in order to create matching distributions of

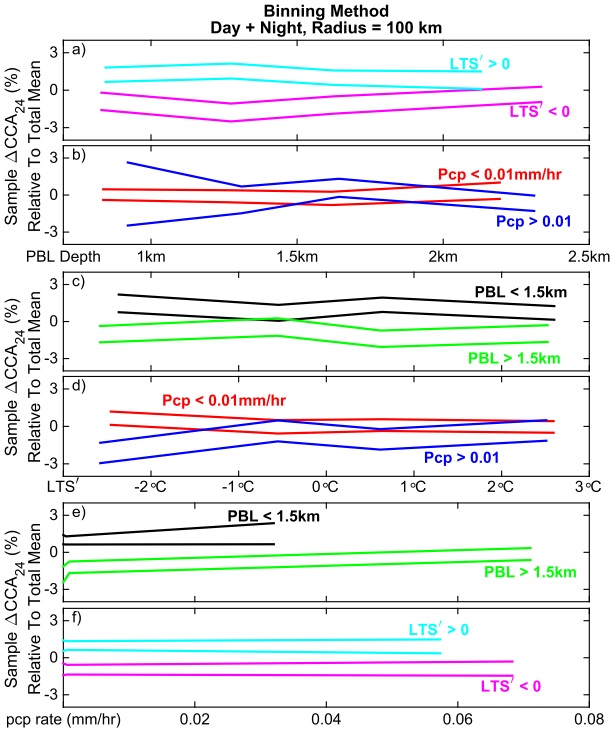

FIG. B3. As in Fig. 11, except here we use a binning method to eliminate the dependence of ΔCCA on initial CCA.

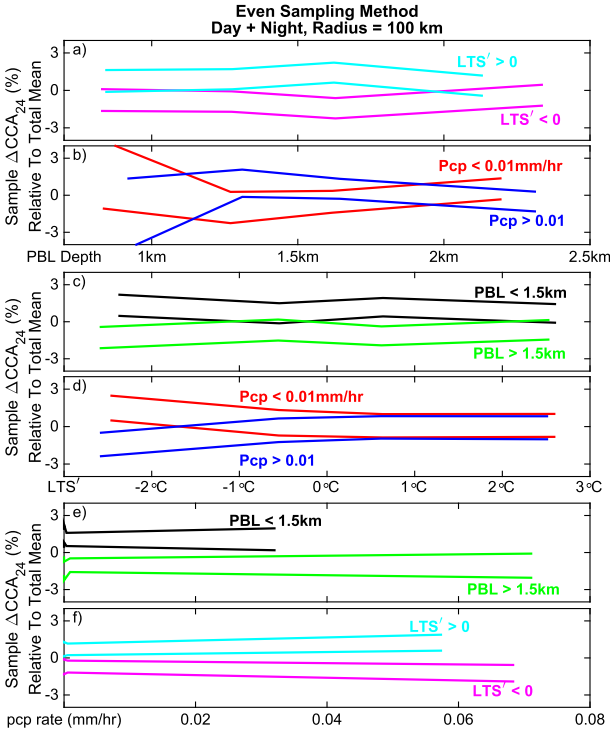

FIG. B4. As in Fig. 11, except here we use an even sampling method to eliminate the dependence of ΔCCA on initial CCA.

initial anomalies [see, e.g., Gryspeerdt et al. (2014), their Fig. 1]. We illustrate this method in Fig. B2, where we show the frequency distributions of initial CCA for trajectories with above- and below-median starting LTS for 20 bins of initial CCA. The dashed line shows the number of comparable observations between the two sets of trajectories. Within each bin we use all available trajectories from the underrepresented subset and randomly sample trajectories from the overrepresented set, forcing the distribution of initial CCAs to match within every bin, thus creating "matched subsets" of trajectories. We can then directly compare the mean ΔCCA between the two matched subsets. We call this method the "even sampling method."

A direct comparison between all three methods shows that they are very consistent for our LTS example. The above-median LTS trajectories show mean ΔCCA values of $+1.01 \pm 0.13$ (linear regression), $+1.01 \pm 0.17$ (binning), and $+0.92 \pm 0.19$ (even sampling), while the below-median LTS trajectories show ΔCCA values of -1.11 ± 0.13 (regression), -1.07 ± 0.18 (binning), and -1.01 ± 0.20 (even sampling).

In the main body of the paper, we choose the linear regression method because the binning method in Fig. B1 still retains some bias: even within the bins the mean initial anomalies are slightly different for the high- and low-LTS groups, leading to a small, but not negligible bias. Although the binning method has the advantage of not assuming linearity, Figs. 8, 10, A2, and A3 show that assuming a linear relationship between initial anomalies and their time changes is reasonable. The even sampling method also produces very similar results, but with a significant loss of data. In our examples above we find consistency between the methods but eroded statistical significance (larger uncertainty bounds) due to the reduced number of available trajectories. In Figs. B3 and B4, we reproduce Fig. 11 using the two alternative methods to show how the results vary between methods.

REFERENCES

Albrecht, B., 1989: Aerosols, cloud microphysics, and fractional cloudiness. *Science*, **245**, 1227–1230, doi:10.1126/science.245.4923.1227.

Bennartz, R., 2007: Global assessment of marine boundary layer cloud droplet number concentration from satellites. *J. Geophys. Res.*, **112**, D02201, doi:10.1029/2006JD007547.

Boers, R., J. A. Acarreta, and J. L. Gras, 2006: Satellite monitoring of the first indirect aerosol effect: Retrieval of the droplet concentration of water clouds. *J. Geophys. Res.*, **111**, D22208, doi:10.1029/2005JD006838.

Bretherton, C. S., and M. Wyant, 1997: Moisture transport, lower-tropospheric stability, and decoupling of cloud-topped

boundary layers. *J. Atmos. Sci.*, **54**, 148–167, doi:10.1175/1520-0469(1997)054<0148:MTLTSA>2.0.CO;2.

——, and Coauthors, 2004: The EPIC 2001 stratocumulus study. *Bull. Amer. Meteor. Soc.*, **85**, 967–977, doi:10.1175/BAMS-85-7-967.

——, R. Wood, R. C. George, D. Leon, G. Allen, and X. Zheng, 2010: Southeast Pacific stratocumulus clouds, precipitation and boundary layer structure sampled along 20° S during VOCALS-Rex. *Atmos. Chem. Phys.*, **10**, 10 639–10 654, doi:10.5194/acp-10-10639-2010.

Burleyson, C. D., and S. E. Yuter, 2015: Subdiurnal stratocumulus cloud fraction variability and sensitivity to precipitation. *J. Climate*, **28**, 2968–2985, doi:10.1175/JCLI-D-14-00648.1.

Comstock, K. K., R. Wood, S. E. Yuter, and C. S. Bretherton, 2004: Reflectivity and rain rate in and below drizzling stratocumulus. *Quart. J. Roy. Meteor. Soc.*, **130**, 2891–2918, doi:10.1256/qj.03.187.

——, C. S. Bretherton, and S. E. Yuter, 2005: Mesoscale variability and drizzle in southeast Pacific stratocumulus. *J. Atmos. Sci.*, **62**, 3792–3807, doi:10.1175/JAS3567.1.

Dee, D. P., and Coauthors, 2011: The ERA-Interim reanalysis: Configuration and performance of the data assimilation system. *Quart. J. Roy. Meteor. Soc.*, **137**, 553–597, doi:10.1002/qj.828.

Eastman, R., and S. G. Warren, 2014: Diurnal cycles of cumulus, cumulonimbus, stratus, stratocumulus, and fog from surface observations over land and ocean. *J. Climate*, **27**, 2386–2404, doi:10.1175/JCLI-D-13-00352.1.

Gryspeerdt, E., P. Stier, and D. G. Partridge, 2014: Satellite observations of cloud regime development: The role of aerosol processes. *Atmos. Chem. Phys.*, **14**, 1141–1158, doi:10.5194/acp-14-1141-2014.

Hahn, C. J., and S. G. Warren, 2007: A gridded climatology of clouds over land (1971-96) and ocean (1954-97) from surface observations worldwide. Department of Energy CDIAC Numeric Data Package NDP-026E, accessed 6 November 2015, doi:10.3334/CDIAC/cli.ndp026e.

Hartmann, D. L., and D. A. Short, 1980: On the use of earth radiation budget statistics for studies of clouds and climate. *J. Atmos. Sci.*, **37**, 1233–1250, doi:10.1175/1520-0469(1980)037<1233:OTUOER>2.0.CO;2.

Hubanks, P. A., M. D. King, S. Platnick, and R. Pincus, 2008: MODIS atmosphere L3 gridded product. NASA Algorithm Theoretical Basis Doc. ATBD-MOD-30, 90 pp.

King, M. D., and Coauthors, 2003: Cloud and aerosol properties, precipitable water, and profiles of temperature and humidity. *IEEE Trans. Geosci. Remote Sens.*, **41**, 442–458, doi:10.1109/TGRS.2002.808226.

Klein, S. A., and D. L. Hartmann, 1993: The seasonal cycle of low stratiform clouds. *J. Climate*, **6**, 1587–1606, doi:10.1175/1520-0442(1993)006<1587:TSCOLS>2.0.CO;2.

——, ——, and J. R. Norris, 1995: On the relationship among low-cloud structure, sea surface temperature and atmospheric circulation in the summertime northeast Pacific. *J. Climate*, **8**, 1140–1155, doi:10.1175/1520-0442(1995)008<1140:OTRALC>2.0.CO;2.

Krueger, S. K., G. T. McLean, and Q. Fu, 1995: Numerical simulation of the stratus-to-cumulus transition in the subtropical marine boundary layer. Part I: Boundary layer structure. *J. Atmos. Sci.*, **52**, 2839–2850, doi:10.1175/1520-0469(1995)052<2839:NSOTST>2.0.CO;2.

Lebsock, M. D., and T. S. L'Ecuyer, 2011: The retrieval of warm rain from CloudSat. *J. Geophys. Res.*, **116**, D20209, doi:10.1029/2011JD016076.

Lilly, D. K., 1968: Models of cloud-topped mixed layers under a strong inversion. *Quart. J. Roy. Meteor. Soc.*, **94**, 292–309, doi:10.1002/qj.49709440106.

Maddux, B. C., S. A. Ackerman, and S. Platnick, 2010: Viewing geometry dependencies in MODIS cloud products. *J. Atmos. Oceanic Technol.*, **27**, 1519–1528, doi:10.1175/2010JTECHA1432.1.

Martin, G. M., D. W. Johnson, and A. Spice, 1994: The measurement and parameterization of effective radius of droplets in warm stratocumulus clouds. *J. Atmos. Sci.*, **51**, 1823–1842, doi:10.1175/1520-0469(1994)051<1823:TMAPOE>2.0.CO;2.

Mauger, G. S., and J. R. Norris, 2010: Assessing the impact of meteorological history on subtropical cloud fraction. *J. Climate*, **23**, 2926–2940, doi:10.1175/2010JCLI3272.1.

Mechem, D. B., and Y. L. Kogan, 2003: Simulating the transition from drizzling marine stratocumulus to boundary layer cumulus with a mesoscale model. *Mon. Wea. Rev.*, **131**, 2342–2360, doi:10.1175/1520-0493(2003)131<2342:STTFDM>2.0.CO;2.

Mitrescu, C., T. L'Ecuyer, J. Haynes, S. Miller, and J. Turk, 2010: *CloudSat* precipitation profiling algorithm: Model description. *J. Appl. Meteor. Climatol.*, **49**, 991–1003, doi:10.1175/2009JAMC2181.1.

Myers, T. A., and J. R. Norris, 2013: Observational evidence that enhanced subsidence reduces subtropical marine boundary layer cloudiness. *J. Climate*, **26**, 7507–7524, doi:10.1175/JCLI-D-12-00736.1.

Nicholls, S., 1984: The dynamics of stratocumulus: Aircraft observations and comparisons with a mixed layer model. *Quart. J. Roy. Meteor. Soc.*, **110**, 783–820, doi:10.1002/qj.49711046603.

——, 1989: The structure of radiatively driven convection in stratocumulus. *Quart. J. Roy. Meteor. Soc.*, **115**, 487–511, doi:10.1002/qj.49711548704.

Oreopoulos, L., 2005: The impact of subsampling on MODIS level-3 statistics of cloud optical thickness and effective radius. *IEEE Trans. Geosci. Remote Sens.*, **43**, 366–373, doi:10.1109/TGRS.2004.841247.

Pincus, R., M. B. Baker, and C. S. Bretherton, 1997: What controls stratocumulus radiative properties? Lagrangian observations of cloud evolution. *J. Atmos. Sci.*, **54**, 2215–2236, doi:10.1175/1520-0469(1997)054<2215:WCSRPL>2.0.CO;2.

Randall, D. A., 1984: Stratocumulus cloud deepening through entrainment. *Tellus*, **36A**, 446–457, doi:10.1111/j.1600-0870.1984.tb00261.x.

Rogers, D. P., and D. Koracin, 1992: Radiative transfer and turbulence in the cloud-topped marine atmospheric boundary layer. *J. Atmos. Sci.*, **49**, 1473–1486, doi:10.1175/1520-0469(1992)049<1473:RTATIT>2.0.CO;2.

Sandu, I., and B. Stevens, 2011: On the factors modulating the stratocumulus to cumulus transitions. *J. Atmos. Sci.*, **68**, 1865–1881, doi:10.1175/2011JAS3614.1.

——, ——, and R. Pincus, 2010: On the transitions in marine boundary layer cloudiness. *Atmos. Chem. Phys.*, **10**, 2377–2391, doi:10.5194/acp-10-2377-2010.

Stevens, B., W. R. Cotton, G. Feingold, and C.-H. Moeng, 1998: Large-eddy simulations of strongly precipitating, shallow, stratocumulus-topped boundary layers. *J. Atmos. Sci.*, **55**, 3616–3638, doi:10.1175/1520-0469(1998)055<3616:LESOSP>2.0.CO;2.

——, G. Vali, K. Comstock, R. Wood, M. VanZanten, P. H. Austin, C. S. Bretherton, and D. H. Lenschow, 2005: Pockets of open cells (POCs) and drizzle in marine stratocumulus. *Bull. Amer. Meteor. Soc.*, **86**, 51–57, doi:10.1175/BAMS-86-1-51.

Terai, C. R., C. S. Bretherton, R. Wood, and G. Painter, 2014: Aircraft observations of aerosol, cloud, precipitation, and boundary layer properties in pockets of open cells over the

southeast Pacific. *Atmos. Chem. Phys.*, **14**, 8071–8088, doi:10.5194/acp-14-8071-2014.

Turton, J. D., and S. Nicholls, 1987: A study of the diurnal variation of stratocumulus using a multiple mixed layer model. *Quart. J. Roy. Meteor. Soc.*, **113**, 969–1009, doi:10.1002/qj.49711347712.

Vaughan, M., S. Young, D. Winker, K. Powell, A. Omar, Z. Liu, Y. Hu, and C. Hostetler, 2004: Fully automated analysis of space-based lidar data: An overview of the CALIPSO retrieval algorithms and data products. *Laser Radar Techniques for Atmospheric Sensing*, U. N. Singh, Ed., International Society for Optical Engineering (SPIE Proceedings, Vol. 5575), 16–30.

Wang, H., and G. Feingold, 2009: Modeling mesoscale cellular structures and drizzle in marine stratocumulus. Part I: Impact of drizzle on the formation and evolution of open cells. *J. Atmos. Sci.*, **66**, 3237–3256, doi:10.1175/2009JAS3022.1.

Wang, S., and B. A. Albrecht, 1986: A stratocumulus model with an internal circulation. *J. Atmos. Sci.*, **43**, 2374–2391, doi:10.1175/1520-0469(1986)043<2374:ASMWAI>2.0.CO;2.

Wentz, F. J., and T. Meissner, 2004: AMSR-E/Aqua L2B global swath ocean products derived from Wentz algorithm, version 2. [L3 LWP]. National Snow and Ice Data Center, Boulder, CO, digital media. [Available online at http://nsidc.org/api/metadata?id=ae_ocean.]

Wood, R., 2000: Parametrization of the effect of drizzle upon the droplet effective radius in stratocumulus clouds. *Quart. J. Roy. Meteor. Soc.*, **126**, 3309–3324, doi:10.1002/qj.49712657015.

——, 2012: Stratocumulus clouds. *Mon. Wea. Rev.*, **140**, 2373–2423, doi:10.1175/MWR-D-11-00121.1.

——, and C. S. Bretherton, 2004: Boundary layer depth, entrainment, and decoupling in the cloud-capped subtropical and tropical marine boundary layer. *J. Climate*, **17**, 3576–3588, doi:10.1175/1520-0442(2004)017<3576:BLDEAD>2.0.CO;2.

——, and D. L. Hartmann, 2006: Spatial variability of liquid water path in marine low cloud: The importance of mesoscale cellular convection. *J. Climate*, **19**, 1748–1764, doi:10.1175/JCLI3702.1.

——, D. Leon, M. Lebsock, J. Snider, and A. D. Clarke, 2012: Precipitation driving droplet concentration variability in low clouds. *J. Geophys. Res.*, **117**, D19210, doi:10.1029/2012JD018305.

Wyant, M. C., C. S. Bretherton, H. A. Rand, and D. E. Stevens, 1997: Numerical simulations and a conceptual model of the stratocumulus to trade cumulus transition. *J. Atmos. Sci.*, **54**, 168–192, doi:10.1175/1520-0469(1997)054<0168:NSAACM>2.0.CO;2.

Xiao, H., C. M. Wu, and C. R. Mechoso, 2011: Buoyancy reversal, decoupling, and the transition from stratocumulus to shallow cumulus topped marine boundary layers. *Climate Dyn.*, **37**, 971–984, doi:10.1007/s00382-010-0882-3.

Zhou, X., P. Kollias, and E. Lewis, 2015: Clouds, precipitation and marine boundary layer structure during the MAGIC field campaign. *J. Climate*, **28**, 2420–2442, doi:10.1175/JCLI-D-14-00320.1.